nature genetics

ARTICLES

https://doi.org/10.1038/s41588-020-0590-9

Using antagonistic pleiotropy to design a chemotherapy-induced evolutionary trap to target drug resistance in cancer

Kevin H. Lin[1,7], Justine C. Rutter[1,7], Abigail Xie[1], Bryann Pardieu[2], Emily T. Winn[3], Reinaldo Dal Bello[2,4], Antoine Forget[2], Raphael Itzykson[2,5], Yeong-Ran Ahn[1], Ziwei Dai[1], Raiyan T. Sobhan[1], Grace R. Anderson[1], Katherine R. Singleton[1], Amy E. Decker[1], Peter S. Winter[1], Jason W. Locasale[1], Lorin Crawford[6], Alexandre Puissant[2,8] ✉ and Kris C. Wood[1,8] ✉

Local adaptation directs populations towards environment-specific fitness maxima through acquisition of positively selected traits. However, rapid environmental changes can identify hidden fitness trade-offs that turn adaptation into maladaptation, resulting in evolutionary traps. Cancer, a disease that is prone to drug resistance, is in principle susceptible to such traps. We therefore performed pooled CRISPR–Cas9 knockout screens in acute myeloid leukemia (AML) cells treated with various chemotherapies to map the drug-dependent genetic basis of fitness trade-offs, a concept known as antagonistic pleiotropy (AP). We identified a PRC2–NSD2/3-mediated MYC regulatory axis as a drug-induced AP pathway whose ability to confer resistance to bromodomain inhibition and sensitivity to BCL-2 inhibition templates an evolutionary trap. Across diverse AML cell-line and patient-derived xenograft models, we find that acquisition of resistance to bromodomain inhibition through this pathway exposes coincident hypersensitivity to BCL-2 inhibition. Thus, drug-induced AP can be leveraged to design evolutionary traps that selectively target drug resistance in cancer.

All populations are subject to selective pressures that enforce local adaptation. In certain cases, the evolved traits that confer local adaptation to a given environment may become maladaptive following changes to that environment[1,2]. These reversals of fortune are known as evolutionary mismatches or evolutionary traps[3,4]. Provided that the environmental shift occurs abruptly enough to evade adaptation and the mismatch is sufficiently large, evolutionary traps can drive local extinction[5].

This concept should be applicable to the construction of two-body chemotherapeutic regimens for the eradication of cancer cell populations. Specifically, local adaptation to chemotherapy could prime an evolutionary trap, which would be triggered upon administration of a carefully selected second drug. This approach is potentially well suited to address the problem of acquired drug resistance in cancer for several reasons. First, acquired drug resistance is often a genetically or epigenetically mediated cell-autonomous process that is selected for in the presence of drug, but could, in principle, be selected against[6–9]. Second, a growing body of evidence suggests that diverse upstream drivers of chemotherapeutic resistance often converge on and activate common effectors, permitting the design of wide-reaching evolutionary traps that exploit recurrent downstream mediators of resistance[7,10–16]. Last, many chemotherapeutic strategies already require multiple drugs to be administered in sequence, allowing for the adoption of evolutionary traps by amending or shuffling existing chemotherapy regimens.

Recognizing this opportunity, a handful of studies have identified 'collateral sensitivities' in cancer cells, scenarios where acquired resistance to an initial therapy produces heightened sensitivity to a second therapy, thus providing the first experimental support for evolutionary traps in cancer[7,13,17]. However, for evolutionary traps to be rationally applied, we require a framework for connecting the specific genetic events that drive acquired drug resistance to the collateral sensitivities that can be used to exploit this resistance. Here, we provide such a framework, producing a genetically coherent model of chemotherapy-induced evolutionary traps.

This framework is built on, and requires an understanding of, drug-induced antagonistic pleiotropy, the concept that genes can exert diametrically opposed effects on fitness in different drug contexts[18,19]. The gold standard method for testing local adaptation and/or AP is reciprocal transplantation, a laborious process that artificially restricts the number of putative AP interactions that can be validated at once[18,19]. To overcome this inefficiency, we used a pooled, loss-of-function CRISPR–Cas9 library targeting major growth, proliferative and oncogenic pathways to screen nine chemotherapies, and effectively performed thousands of reciprocal transplantation experiments in parallel. This approach allowed us to produce a systematic analysis of drug-induced AP, which we used to design an evolutionary trap that subverts acquired drug resistance. The principles described here should be broadly applicable, both for the phenomenological study of AP in cancer and for the rational

[1]Department of Pharmacology and Cancer Biology, Duke University, Durham, NC, USA. [2]Université de Paris, Génomes, Biologie Cellulaire et Thérapeutique U944, INSERM, CNRS, Paris, France. [3]Division of Applied Mathematics, Brown University, Providence, RI, USA. [4]Department of Hematology, Universidade Federal do Rio de Janeiro, Rio de Janeiro, Brazil. [5]Service Hématologie Adultes, AP-HP, Hôpital Saint-Louis, Paris, France. [6]Department of Biostatistics, Brown University, Providence, RI, USA. [7]These authors contributed equally: Kevin H. Lin, Justine C. Rutter. [8]These authors jointly supervised this work: Kris C. Wood, Alexandre Puissant. ✉e-mail: alexandre.puissant@inserm.fr; kris.wood@duke.edu

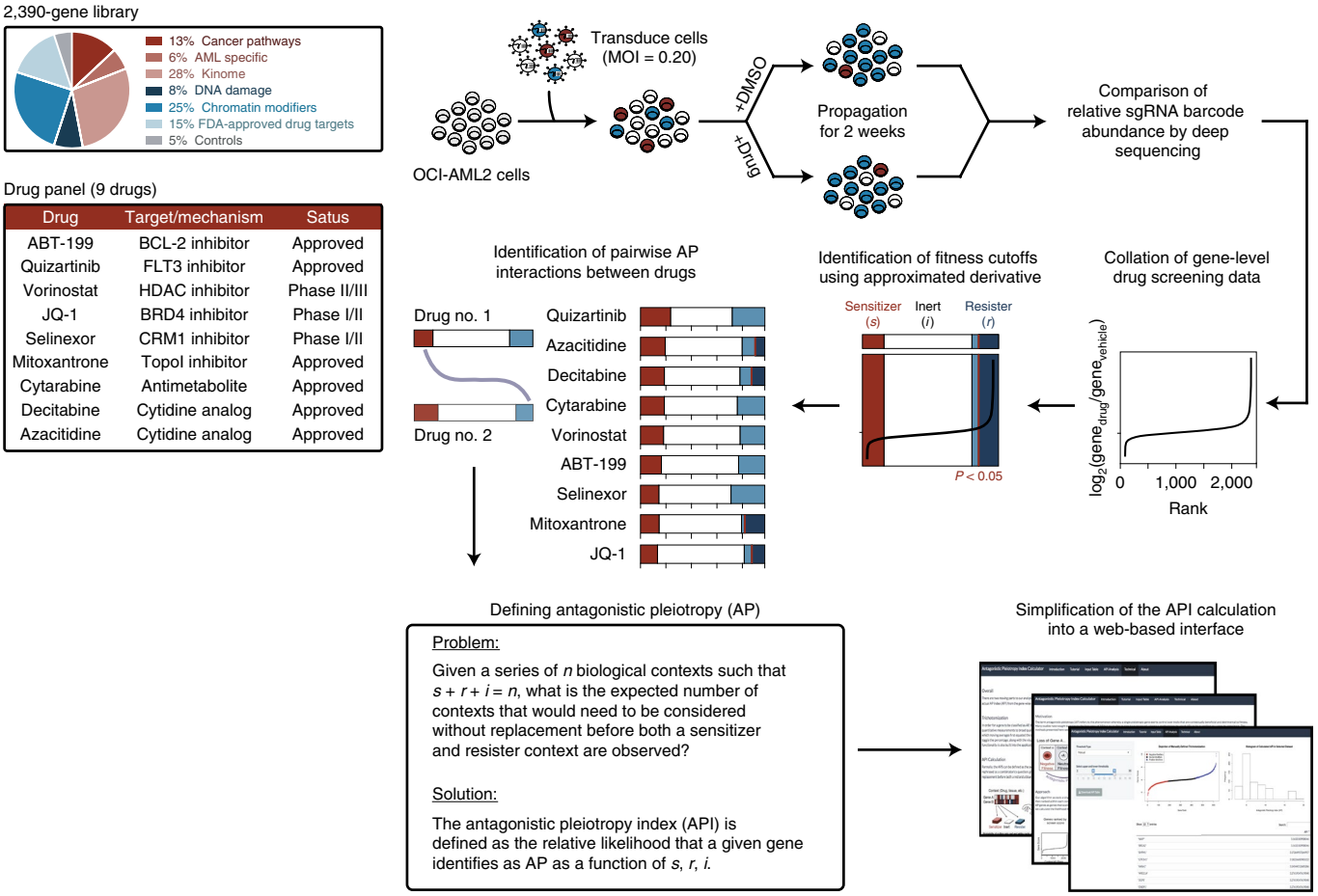

Fig. 1 | Loss-of-function CRISPR screens identify drug-induced antagonistic pleiotropy. Pooled drug-modifier CRISPR–Cas9 screening and API analysis strategy. CRISPR–Cas9 drug-modifier screens represented as fractions of sensitizer (red), inert (white) and resister (blue) genes. Gene cutoffs controlled by *P* value of 0.05. MOI, multiplicity of infection.

construction of chemotherapy-driven evolutionary traps designed to address acquired drug resistance.

Results

Using loss-of-function genetics to identify drug-induced AP. To identify genes that exhibit drug-induced AP, we assembled a CRISPR–Cas9 loss-of-function library composed of 11,200 short guide RNA (sgRNA) constructs targeting 2,240 genes from major cellular and oncogenic signaling pathways, as well as 50 nontargeting constructs and 750 constructs targeting 150 control genes, chosen for their predicted dispensability or essentiality (Supplementary Table 1)[20]. This library was cloned into a published lentiviral system[21] and used to screen a panel of nine chemotherapies in AML cells as previously described[22]. In brief, cells were transduced with library lentivirus, selected with puromycin, treated with vehicle or drug, sampled at 0 and 2 weeks and deconvoluted with deep sequencing (Fig. 1). The compositional abundance of sgRNAs in each drug-treated population was compared to that of the untreated population. Construct scores were averaged into gene scores (Methods and Supplementary Tables 2 and 3).

We sought to identify the AP genes within these drug-modifier screens. A minimal demonstration of drug-induced AP requires that a gene score as a sensitizer to at least one drug (gene loss potentiates drug effect; depleted representation) and as a resister to at least one drug (gene loss refutes drug effect; replete representation). Because it is difficult to impose equivalent selection pressures using different drugs, we used the topology of each drug screen to define fitness thresholds. In brief, genes from each drug screen, ranked from fitness loss to fitness gain, were trichotomized by imposing two cutoffs, distinguishing fitness loss from inertness and inertness from fitness gain (Methods). These cutoffs were evaluated against the distribution of nontargeting control genes and controlled at $P<0.05$. The resulting drug-induced, gene-level designations were used to define three types of pairwise gene–gene interactions within the drug-treated datasets: sensitizer–sensitizer (shared detriment), resister–resister (shared benefit) and sensitizer–resister interactions. Sensitizer–resister interactions are particularly notable because they represent examples of drug-induced AP, namely, instances where loss of a gene confers a fitness benefit in the presence of one drug and a fitness penalty in the presence of another. After application of this generous definition of drug-induced AP to our data, nearly half of the genes (1,174 of 2,390 genes) in our library were classified as having AP.

Defining an antagonistic pleiotropy index. To prioritize genes by the strength of their drug-induced AP properties, we formalized an antagonistic pleiotropy index (API) expressed in terms of the total number of contexts (n) and the number of contexts in which a gene is classified as a sensitizer (s), resister (r) or inert (i). An analytical solution can be obtained by solving the following problem: given a series of contexts, such that $s+r+i=n$, what is the expected number of contexts without replacement before both sensitizer and resister contexts are observed, thus qualifying the gene as having AP? A solution to this problem is provided (Supplementary Note)

in which the genes most likely to be observed as AP have the lowest API, and vice versa.

To validate the basic functions of the API, we reanalyzed two publicly available datasets. These analyses serve to affirm the basic functions of the API and provide an intuitive understanding for the quantification of AP (Supplementary Note and Extended Data Fig. 1a–k). To facilitate adoption of the API, we have provided a web interface (https://apicalculator.shinyapps.io/api_shiny_directory/) that users can use to analyze their own datasets.

Analyzing drug-treated screens using API. Next, we applied the API to our drug-modifier screens (Extended Data Fig. 2a and Supplementary Table 4). Ontology analysis of the top AP genes, defined as API < 4.5 (348 genes, top 15%; Supplementary Table 4), showed enrichment for transcriptional and epigenetic modifiers (Extended Data Fig. 2b). This coheres with the notion that chromatin modifications can drive both drug tolerance and chemosensitivity in cancer cells[23–26].

To map the connections between fitness-detrimental and fitness-beneficial genes, we arranged our CRISPR screens circumferentially as segments of a circos plot, with the segments connected to each other through links representing shared chemosensitizers or chemoresisters (Fig. 2a and Extended Data Fig. 2c). Within each drug pair our analysis identified genes that were fitness-detrimental in the presence of one drug and fitness-beneficial for another—AP genes (Fig. 2a). The linkage patterns that connected drug tracts to one another uncovered broad trends. For instance, decitabine, azacitidine and JQ-1 share many fitness-detrimental and fitness-beneficial genes but few AP genes, which is consistent with principal component analysis (PCA) of the screens (Extended Data Fig. 2d).

Importantly, screens also resolved differences between drugs. Azacitidine requires activation by uridine-cytidine kinase 2 (encoded by *UCK2*)[27] while its deoxy derivative, decitabine, is activated by deoxycytidine kinase (encoded by *DCK*)[28,29]. Both genes scored strongly as resisters in their respective drug screens, and inertly in the other drug screens (Extended Data Fig. 2e). Accordingly, the screen conducted with cytarabine, a deoxycytidine antimetabolite that shares structural similarities with decitabine, identified DCK as a resister, and the equilibrative nucleoside transporter hENT1 (encoded by *SLC29A1*), which is required for uptake of deoxycytidines[29], scored as a strong resister in the decitabine and cytarabine screens, but not in the azacitidine screen (Extended Data Fig. 2e–j).

The PRC2 complex and NSD2/3 comprise an AP axis. Next, we evaluated each of the 36 possible drug pairs for their shared sensitizer, resister and AP interactions across the set of top AP genes (API < 4.5) (Fig. 2b). We observed wide variation in the composition of shared interactions across drug pairs. For instance, the hypomethylating agents decitabine and azacitidine harbored few AP interactions, along with the highest percentage of shared sensitizer interactions. In contrast, there were many AP interactions between ABT-199 and both decitabine and azacitidine, which stood apart from pairwise relationships identified using PCA or correlative analyses (Extended Data Fig. 3a,b). We validated an exemplar AP axis composed of *KDM1A* (encoding LSD1) and known LSD1 regulators repressor element-1 silencing transcription factor corepressors 1, 2 and 3 (*RCOR1/2/3*) (Fig. 2c–f). Additional development of *KDM1A* as an AP gene can be found in the Supplementary Note and Extended Data Fig. 4a–i.

Among the drug pairs, ABT-199 and JQ-1 recorded the highest percentage of AP interactions, suggesting that the resister and sensitizer landscapes of these drugs were most opposed (Fig. 2b). In particular, we identified four AP genes that were unified on the basis of their reciprocal transcriptional regulation. *EZH2* (API = 4.2) and *EED* (API = 3.9), which encode components of PRC2, a gene silencing complex that catalyzes H3K27 trimethylation[30,31], scored as sensitizers in the ABT-199 screen; *EED* also scored as a resister in the JQ-1 screen (Fig. 2g and Extended Data Fig. 5a). The transcriptionally repressive H3K27me3 marks deposited by PRC2 are opposed by transcriptionally activating H3K36me1/2 marks[32,33]. Accordingly, two H3K36 methyltransferases, NSD2 (API = 3.3) and NSD3 (API = 4.7)[34] scored in opposition to the PRC2 members (Fig. 2g and Extended Data Fig. 5a). While these findings were consistent, it was unclear why these epigenetic modifiers should modulate the effect of these two drugs. To find possible effectors, we canvassed our dataset for genes that behaved like *EZH2*/*EED* or *NSD2*/*NSD3* in the ABT-199 and JQ-1 screens. Our search identified the transcription factor MYC, which scored alongside *NSD2/3* and opposite *EZH2/EED* in the ABT-199 and JQ-1 screens (Fig. 2g and Extended Data Fig. 5a). These correlations agree with previous studies, which describe the negative transcriptional control of MYC by PRC2 (ref. [35]), and together delineate an AP axis featuring the reciprocal regulation of MYC by NSD2/3 and EZH2/EED (PRC2; Fig. 2g).

EZH2/EED counterpoise NSD2/3 at the level of MYC. To investigate the capacity of MYC to affect drug sensitivity, we performed knockdown and overexpression studies. Compared to cells expressing scrambled short hairpin RNAs (shRNAs), cells expressing *MYC*-targeting shRNAs were sensitized to JQ-1 and resistant to ABT-199 (Fig. 2h,i and Extended Data Fig. 5b–e). Reciprocally, overexpression of MYC conferred resistance to JQ-1 and sensitized cells to ABT-199 (Fig. 2j,k and Extended Data Fig. 5f–i). Taken alongside data from the screen, these studies validated the sufficiency of MYC to modulate drug sensitization (Fig. 3a).

Next, we tested the capacity of CRISPR–Cas9-mediated *NSD2/3* and *EZH2* knockout to modulate MYC and sensitivity to JQ-1 and ABT-199. *NSD2/3* knockout resulted in reduction of *MYC* mRNA (Fig. 3b and Extended Data Fig. 6a,b) and sensitization to JQ-1 (Fig. 3c and Extended Data Fig. 6c). Short-term MYC-suppressive sensitization to JQ-1 is slight because JQ-1 treatment acutely suppresses MYC, leaving little room for additional downregulation. Conversely, knockout of *EED* or *EZH2* increased *MYC* mRNA (Fig. 3d and Extended Data Fig. 6d,e) and sensitized AML cells to ABT-199 (Fig. 3e and Extended Data Fig. 6f). These effects were mimicked by using the EZH2 inhibitors GSK-126 in vitro (Fig. 3f,g) and EPZ-6438 in NSG-SGM3 (NSGS) mice xenografted with patient-derived AML cells (Fig. 3h).

To determine whether PRC2–NSD2/3–MYC-driven resistance arises from chronic drug treatment, we cultured OCI-AML2 cells in escalating doses of ABT-199 or JQ-1 until they exhibited drug resistance (Fig. 3i and Extended Data Fig. 7a). Western blot analysis showed that, compared to cells cultured in DMSO, ABT-199-resistant OCI-AML2 cells did not exhibit changes in MYC (Extended Data Fig. 7b); rather, previous studies have shown that resistance to ABT-199 often relies on upregulation of BCL-X_L and MCL-1 (refs. [36,37]). However, JQ-1-resistant OCI-AML2 cells upregulated MYC at the protein level (Fig. 3j). This prompted us to culture four additional AML cell lines in the presence of JQ-1 until resistance was achieved (Fig. 3i). In each case, the acquisition of JQ-1 resistance was associated with MYC upregulation, suggesting that MYC upregulation is a pervasive feature of acquired JQ-1 resistance in AML (Fig. 3j).

Subsequently, we sought to characterize the means of MYC upregulation. Quantitative PCR with reverse transcription (qRT–PCR) analysis showed a relative increase in *MYC* transcripts in all but one model (Extended Data Fig. 7c), which is consistent with epigenetic regulation and potential involvement of the PRC2–NSD2/3–MYC axis. Protein levels of NSD2 and NSD3 were not increased in any of the resistant lines (Extended Data Fig. 7d). However, two of the JQ-1-resistant lines displayed a reduction in

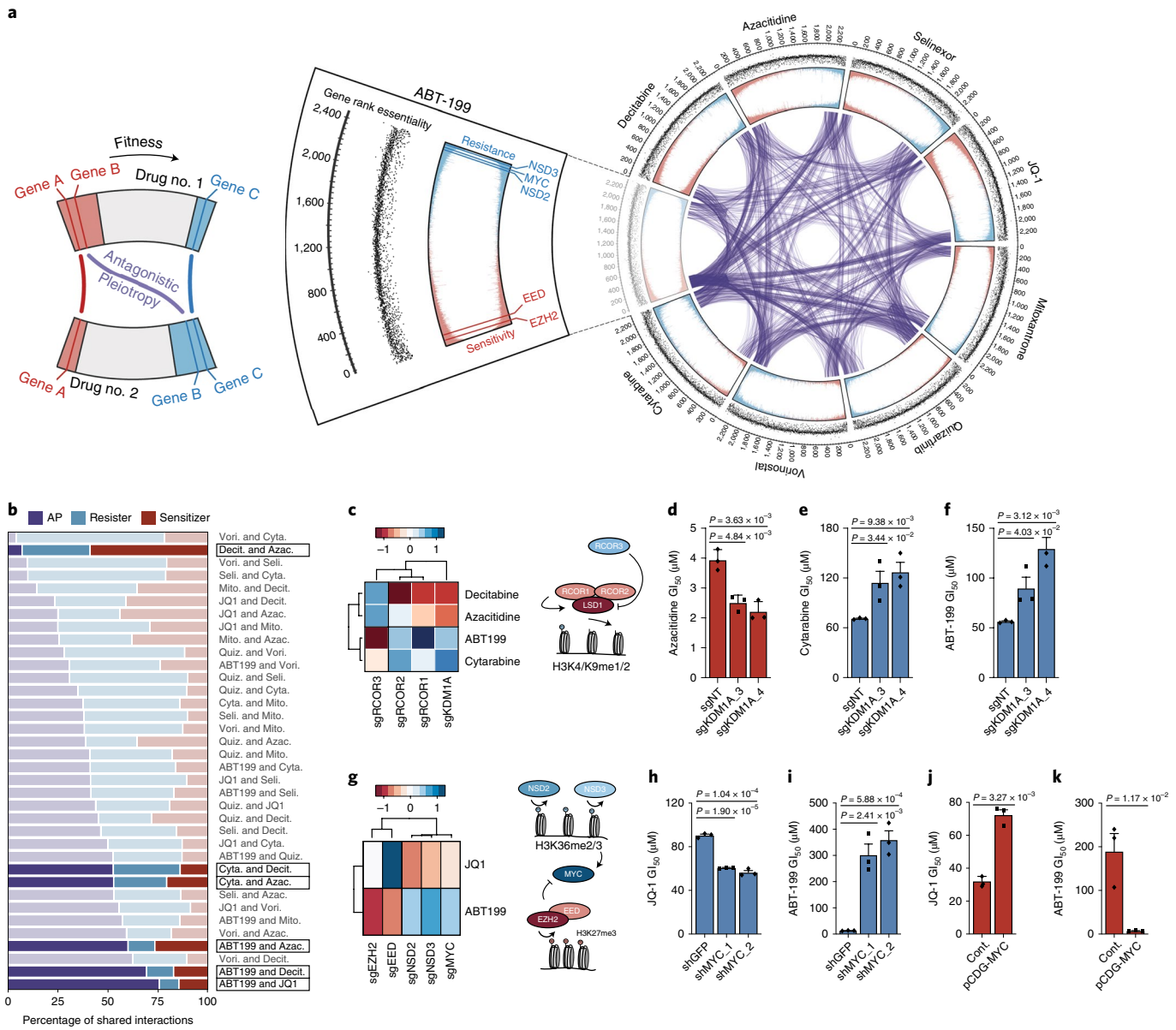

Fig. 2 | Analysis of drug-induced antagonistic pleiotropy reveals gene–gene and drug–drug interactions. a, Circos plot displaying data from drug-modifier CRISPR screens. The screen conducted in the presence of ABT-199 is shown as a cutout with annotations from the outermost rim: genes ranked from most sensitizing (rank = 1) to most resisting (rank = 2,390); scatter plot of corresponding gene essentiality score; drug-modifier score (shown in replicate), colored to depict sensitizers (red) and resisters (blue). Gene–gene relationships that exhibit AP between drug screens are indicated by purple connections. **b**, Breakdown of shared sensitizer, shared resister and AP gene interactions between 36 drug pairs. Drug pairs are ranked by percentage of AP gene interactions. **c**, Heat map representing the effect of sgRNAs targeting *KDM1A* (encoding LSD1) and *RCOR1/2/3* ($n = 5$ sgRNAs per gene) on ABT-199, cytarabine, decitabine and azacitidine; schematic depicts the known relationship between genes identified in the screen. **d**–**f**, GI_{50} values of azacitidine (**d**), cytarabine (**e**) and ABT-199 (**f**) in OCI-AML2 cells following CRISPR–Cas9-mediated knockout of *KDM1A* versus nontargeting control. **g**, Heat map representing the effect of sgRNAs targeting *MYC*, *NSD2/3*, *EED*, *EZH2* ($n = 5$ sgRNAs per gene) on JQ-1 and ABT-199 from CRISPR–Cas9 screens; schematic depicts the reciprocal effects of NSD2/3 and EED, EZH2 on their respective methylation marks and, indirectly, MYC. **h**,**i**, GI_{50} values of JQ-1 (**h**) and ABT-199 (**i**) following short-hairpin knockdown of *MYC* versus shGFP. **j**,**k**, GI_{50} values of JQ-1 (**j**) and ABT-199 (**k**) following overexpression of pCDH-MYC versus control vector. **d**–**f**,**h**–**k**, *P* values computed by two-sided *t*-test for equal means. Data are presented as mean ± s.e.m. for $n = 3$ biologically independent experiments.

EZH2 protein (Fig. 3j), in line with MYC upregulation and a role for EZH2 loss in JQ-1 resistance. Those lines also exhibited collateral resistance to the bromodomain and extra-terminal family protein degrader ARV771 (Extended Data Fig. 7e,f), suggesting that control of MYC expression may have shifted from BRD4 to EZH2 loss in these JQ-1-resistant cells. To test this, we overexpressed GFP or EZH2 in parental and JQ-1-resistant OCI-AML2 lines. In parental cells, EZH2 overexpression increased global H3K27me3 without substantially affecting MYC expression or cell viability (Fig. 3k,l). In contrast, EZH2 overexpression in resistant cells led to increased global H3K27me3, loss of MYC protein and loss of cellular viability (Fig. 3k,l), implying that upregulation of MYC was now dependent on EZH2 loss. Mechanistically, western blot analysis of JQ-1-resistant OCI-AML2 cells identified an increase in CDK1-mediated phosphorylation of EZH2 at Thr487 (Extended Data Fig. 7g), a ubiquitin-dependent phosphodegron[38]. Immunoprecipitation of

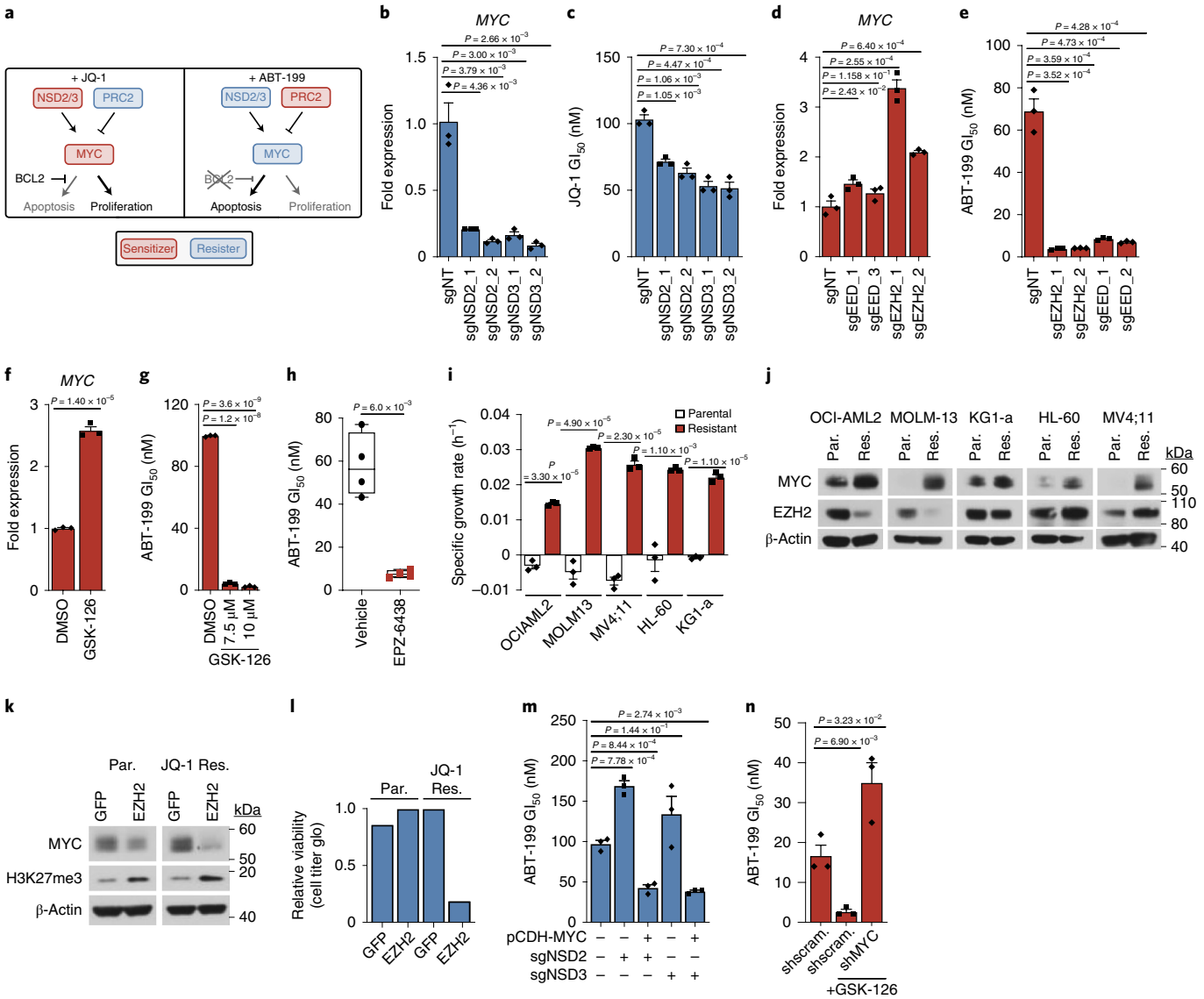

Fig. 3 | MYC and its epigenetic regulators are drug-induced AP genes. a, Schematic depicting drug-dependent polarity of the MYC axis, as defined by drug-modifier screens. **b**,**c**, Effect of sgRNAs targeting *NSD2* or *NSD3* versus nontargeting control in OCI-AML2 cells on *MYC* transcripts (**b**) and JQ-1 GI_{50} (**c**). **d**,**e**, Effect of sgRNAs targeting *EED* or *EZH2* versus nontargeting control in OCI-AML2 cells on MYC transcripts (**d**) and ABT-199 GI_{50} (**e**). **f**, Fold change of *MYC* transcripts following 48-h treatment with EZH2 inhibitor GSK-126. **g**, ABT-199 GI_{50} combined with GSK-126 in OCI-AML2. **h**, ABT-199 GI_{50} values from drug-naïve and EPZ-6438-relapsed AML PDX cells. $hCD45^+$ blasts from whole bone marrow were subjected to 72-h ABT-199 incubation. Significance determined by Welch's two-sample *t*-test. Box plot elements are defined in the Methods. Data are mean ± s.e.m. of $n = 4$ biologically independent animals. **i**, Specific growth rate in the presence of JQ-1 in matched parental and JQ-1-resistant AML cell lines. Representative growth rate of $n = 4$ independent samplings. **j**, Immunoblot analysis of MYC and EZH2 across matched parental (Par.) and JQ-1-resistant (Res.) AML cell lines. Representative immunoblot of $n = 3$ independent experiments. **k**, Immunoblot analysis of MYC and H3K27me3 following overexpression of GFP control and EZH2 in parental and JQ-1-resistant OCI-AML2 cells. Representative immunoblot of $n = 3$ independent experiments. **l**, Relative cell viability of parental and JQ-1-resistant OCI-AML2 cells following overexpression of GFP control or EZH2 for $n = 1$ biologically independent experiments. **m**, ABT-199 GI_{50} following overexpression of pCDH-MYC in *NSD2/3* knockout cells. **n**, ABT-199 GI_{50} following short-hairpin knockdown of *MYC* versus scrambled (scram.) control. **b**–**g**,**i**,**m**,**n**, *P* values computed by two-sided *t*-test for equal means. Data are mean ± s.e.m. for $n = 3$ biologically independent experiments. Uncropped blots are provided in the Source Data.

EZH2 showed increased bound ubiquitin (Extended Data Fig. 7h). Inhibition of CDK1 or the proteasome was sufficient to rescue EZH2 in JQ-1-resistant OCI-AML2 cells (Extended Data Fig. 7i).

Because we did not observe transcriptional upregulation of MYC in all JQ-1-resistant models, we reasoned that other modes of regulation also played a role. MYC is known to be the object of successive phosphorylation events catalyzed by ERK and GSK3β, the latter of which is controlled by AKT and whose phosphorylation of MYC permits consequent ubiquitination and proteolysis[39]. To explore this paradigm in our models, we performed cycloheximide chase experiments on each parental-resistant pair, finding a relative increase in MYC stability in three out of five resistant lines (Extended Data Fig. 8a,b). Those lines exhibited evidence of AKT and ERK activation by western blot (Extended Data Fig. 8c), while the two lines with unchanged MYC stability did not have increased AKT or ERK signaling. Furthermore, MYC was more sensitive to

ERK inhibition in AKT/ERK-active resistant models than in their parental counterparts (Extended Data Fig. 8d), which is consistent with an increased dependence on AKT/ERK signaling. These resistant models were also sensitive to the combination of JQ-1 and ERK inhibition (Extended Data Fig. 8e,f). These data indicate that transcriptional and posttranslational regulation of MYC can jointly account for the MYC upregulation observed in our JQ-1-resistant models, although additional mechanisms cannot be excluded.

Together, these data demonstrate that MYC upregulation is a common feature of JQ-1-resistant AML cells and that this upregulation can be driven by dysregulation of the PRC2–NSD2/3–MYC regulatory axis nominated through our AP analysis. Finally, to establish that the effects of NSD2/3 loss or EZH2 inhibition on ABT-199 sensitivity were mediated through MYC, we sought to rescue their observed effects by overexpressing or knocking out MYC. In NSD2/3 knockout cells, overexpression of MYC restored sensitivity to ABT-199 (Fig. 3m and Extended Data Fig. 8g–i). Correspondingly, sensitization to ABT-199 mediated by EZH2 inhibition was rescued by MYC knockdown (Fig. 3n). These observations point to MYC upregulation as the basis for the synergy between EZH2 and BCL-2 inhibition that we observe here in AML, and previously described in non-Hodgkin's lymphoma [40].

MYC upregulation sensitizes to BH3 mimetics. Up to this point, our data assert that the pleiotropic effects of MYC on cellular growth and death allow it to assume one of two roles: its incumbent oncogenic, proproliferative role, which is observed in most cancer-related contexts, or a proapoptotic role, which is unmasked in the presence of BH3 mimetics or circumstances that otherwise compromise the antiapoptotic machinery of the cancer cell. This duality, which is capable of subverting the effects of one drug while abetting another, should empower MYC to act as the driving mechanism for an evolutionary trap. However, to realize the trap, it is essential to determine whether MYC-driven resistance gives rise to enhanced sensitivity to BCL-2 inhibition.

To investigate this, we tested the sensitivity of our JQ-1-resistant AML cell-line models to ABT-199. Each JQ-1-resistant model was markedly more sensitive to ABT-199 than to its parental counterpart (in contrast, ABT-199-resistant cells were not sensitized to JQ-1; Fig. 4a and Extended Data Fig. 9a). The collateral sensitivity to ABT-199 was MYC dependent and rescuable by shRNA-mediated MYC knockdown (Fig. 4b and Extended Data Fig. 9b). Both resistance to JQ-1 and collateral sensitivity to ABT-199 were stable following removal of JQ-1 for 10 d (Extended Data Fig. 9c–f). Having demonstrated that parallel evolution converges upon MYC as an adaptive mechanism of resistance to JQ-1, the finding that MYC upregulation is responsible for heightened sensitivity to ABT-199 qualifies it to act as the functional requisite of an evolutionary trap: an adaptive response to an initial selective pressure (JQ-1) that is rendered maladaptive by a successive selective pressure (ABT-199).

To understand the mechanism of acquired sensitivity to ABT-199, we performed BH3 profiling[41] on each parental-resistant pair. JQ-1-resistant cells exhibited increased mitochondrial depolarization when acquainted with BCL-2-like protein 11 (BIM) and/or BH3 interacting-domain death agonist (BID; Fig. 4c). This suggested that the JQ-1-resistant cells were more primed for intrinsic, mitochondrial apoptosis than their parental counterparts. Such a state signals a shift in the balance of proapoptotic versus antiapoptotic BCL-2 family members. Expression analysis of BCL-2 family members showed an increase in BIM in each JQ-1-resistant derivative compared to its parental pair (Fig. 4d and Extended Data Fig. 9g), which is consistent with BIM upregulation secondary to MYC overexpression (Extended Data Fig. 9h), and the fact that *BIM* is an established, direct transcriptional target of MYC[42–44]. CRISPR-mediated knockout of *BIM* neutralized the sensitivity to ABT-199 observed in JQ-1-resistant cells (Fig. 4e and Extended Data Fig. 9i). Notably, MYC upregulation was not associated with consistent alterations in other BCL-2 family proteins, including NOXA and PUMA, known p53 targets that can be indirectly activated by MYC through p19, and the antiapoptotic proteins BCL-2, MCL-1 and BCL-X_L (Fig. 4d)[45,46].

Having established that BIM upregulation was the means for the observed collateral sensitivity to ABT-199, we reasoned that upregulation of a proapoptotic protein like BIM should sensitize to other BCL-2 family inhibitors and proapoptotic chemotherapeutics[47]. We examined this by profiling JQ-1-resistant OCI-AML2 cells and their vehicle-treated counterparts, by using a panel of 40 chemotherapies (Fig. 4f and Extended Data Fig. 9j). Here, we observed a general shift toward sensitivity in the JQ-1-resistant cells. Among the drugs that elicited a potentiated response in JQ-1-resistant cells were BH3 mimetics: ABT-199, WEHI-539, the selective MCL-1 inhibitor S63845 and the combined BCL-2/BCL-X_L inhibitor ABT-737 (Fig. 4g). We also noticed hypersensitivities to inhibitors of aurora kinase A (CYC116), glutaminase (BPTES) and lactate dehydrogenase (FX11), each of which has been implicated as a synthetic dependency of oncogenic MYC (Fig. 4f,g and Extended Data Fig. 9j)[48–50]. Thus, many of the collateral sensitivities observed in JQ-1-resistant cells are associated with MYC, either as a requirement for MYC dependence or related to apoptotic priming from MYC-driven BIM upregulation.

Finally, the notion that MYC-driven resistance to JQ-1 lays an evolutionary trap that can be deployed in AML through treatment with BH3 mimetics suggests that a similar approach could be used in other acquired resistance models, particularly given the emerging role of MYC as a widespread mediator of acquired resistance to targeted therapies[7,51–56]. To test this concept, we evolved a panel of cell lines from distinct lineages and harboring different driver mutations to resistance to their cognate inhibitors (Fig. 4h and Extended Data Fig. 9k–p). Across all models, we observed that drug resistance associated with MYC upregulation was accompanied by collateral sensitivities to BH3 mimetics, while MYC-independent models were indifferent to BH3 mimetic treatment (Fig. 4h and Extended Data Fig. 9k–p). This was true even when considering distinct drug-resistant clones derived from the same parental population but exhibiting variable MYC expression. Collectively, these data suggested that the principles described and defined here in AML cells are generalizable and robust to tissue-specific variation. Furthermore, these findings imply that solid tumors, which are largely thought to be insensitive to BH3 mimetics, can be primed for apoptosis by MYC upregulation and rendered vulnerable to MYC-dependent evolutionary traps.

Validating the evolutionary trap in a patient-derived xenograft (PDX) model of AML. To determine whether a MYC-dependent evolutionary trap could be therapeutically exploited, we asked whether JQ-1 treatment of a PDX model of AML could prime cells for apoptosis in a BCL-2-dependent manner. First, we engrafted NSGS mice with an AML PDX and treated with JQ-1 for 10 d. Engrafted PDX cells were collected after resurgence of leukemia in the peripheral blood. BH3 profiling showed that the relapsed JQ-1-treated PDX cells exhibited BCL-2-dependent priming, evidenced by the potentiated release of cytochrome *c* upon treatment with ABT-199 in JQ-1-treated cells compared to JQ-1-naïve cells (Fig. 5a). The same relapsed JQ-1-treated PDX cells were also more sensitive to ABT-199 in vitro, corroborating data from cell-line models (Fig. 5b). By comparison, treatment with the MCL-1 inhibitor S63845 and the BCL-X_L inhibitor A1331852 elicited the same amount of cytochrome *c* release in JQ-1-treated and JQ-1-naïve cells, suggesting a dominant role for BCL-2 in this model.

Given that in vivo JQ-1 treatment primes AML cells in a BCL-2-dependent manner, increasing in vitro sensitivity to ABT-199, we predicted that murine PDX models treated with JQ-1 would

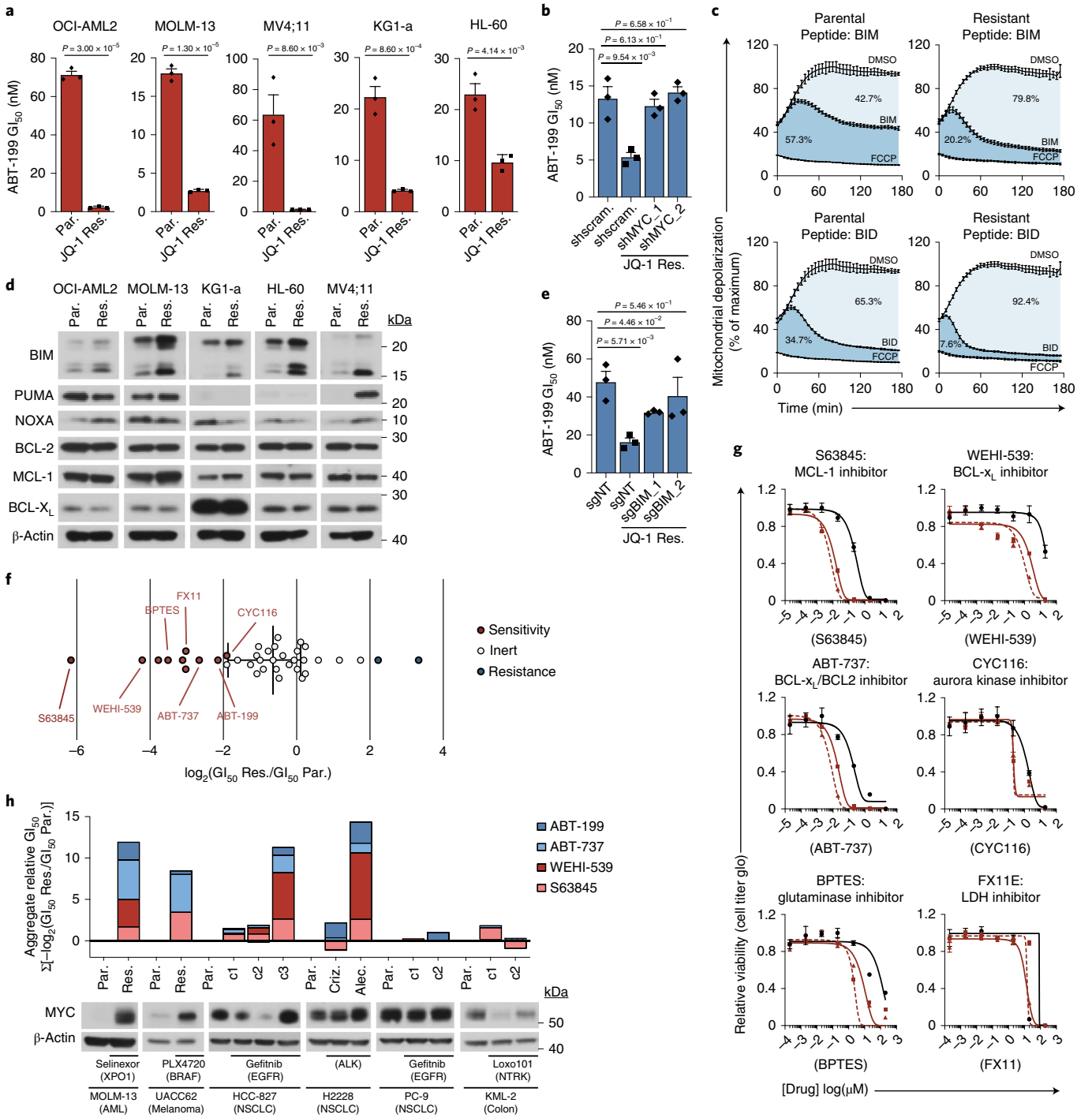

Fig. 4 | MYC upregulation enables a drug-induced evolutionary trap. a, ABT-199 GI_{50} in matched parental and JQ-1-resistant AML cell lines. **b**, ABT-199 GI_{50} in parental and JQ-1-resistant OCI-AML2 cells following short-hairpin knockdown of MYC or scrambled control. **c**, BH3 profiling traces of parental and JQ-1-resistant OCI-AML2 cells stimulated with BIM or BID peptides. Mitochondrial potential was measured every 2 min over 3 h. Percentage depolarization relative to maximal depolarization by carbonyl cyanide-4-(trifluoromethoxy)-phenylhydrazone (FCCP). Data are mean ± s.e.m. for $n = 3$ biologically independent experiments. **d**, Immunoblot analysis of BIM, PUMA, NOXA, BCL-2, MCL-1 and BCL-X_L protein levels across matched parental and JQ-1-resistant AML cell lines. Representative immunoblot of $n = 3$ independent experiments yielding similar results. **e**, ABT-199 GI_{50} in parental and JQ-1-resistant OCI-AML2 cells following CRISPR–Cas9 knockout of BIM or nontargeting control. **f**, $\log_2$ (fold change) in GI_{50} values from 40 compound screen of JQ-1-resistant OCI-AML2 cells relative to parental cells. **g**, Relative cell viability of matched parental and JQ-1-resistant OCI-AML2 cells following 72-h incubation with indicated drugs across an eight-point drug dilution series. Data are mean ± s.e.m. for $n = 3$ biologically independent experiments. **h**, Aggregate $-\log_2(GI_{50})$ of drug-resistant versus parental cell lines, summed across four different BH3 mimetics. Distinct resistant clones marked c1–c3. Data are matched to corresponding MYC immunoblots. Representative immunoblots of $n = 3$ independent experiments yielding similar results. **a**,**b**,**e**, *P* values computed by two-sided *t*-test for equal means. Data are presented as mean ± s.e.m. for $n = 3$ biologically independent experiments. Uncropped blots in are provided in the Source Data.

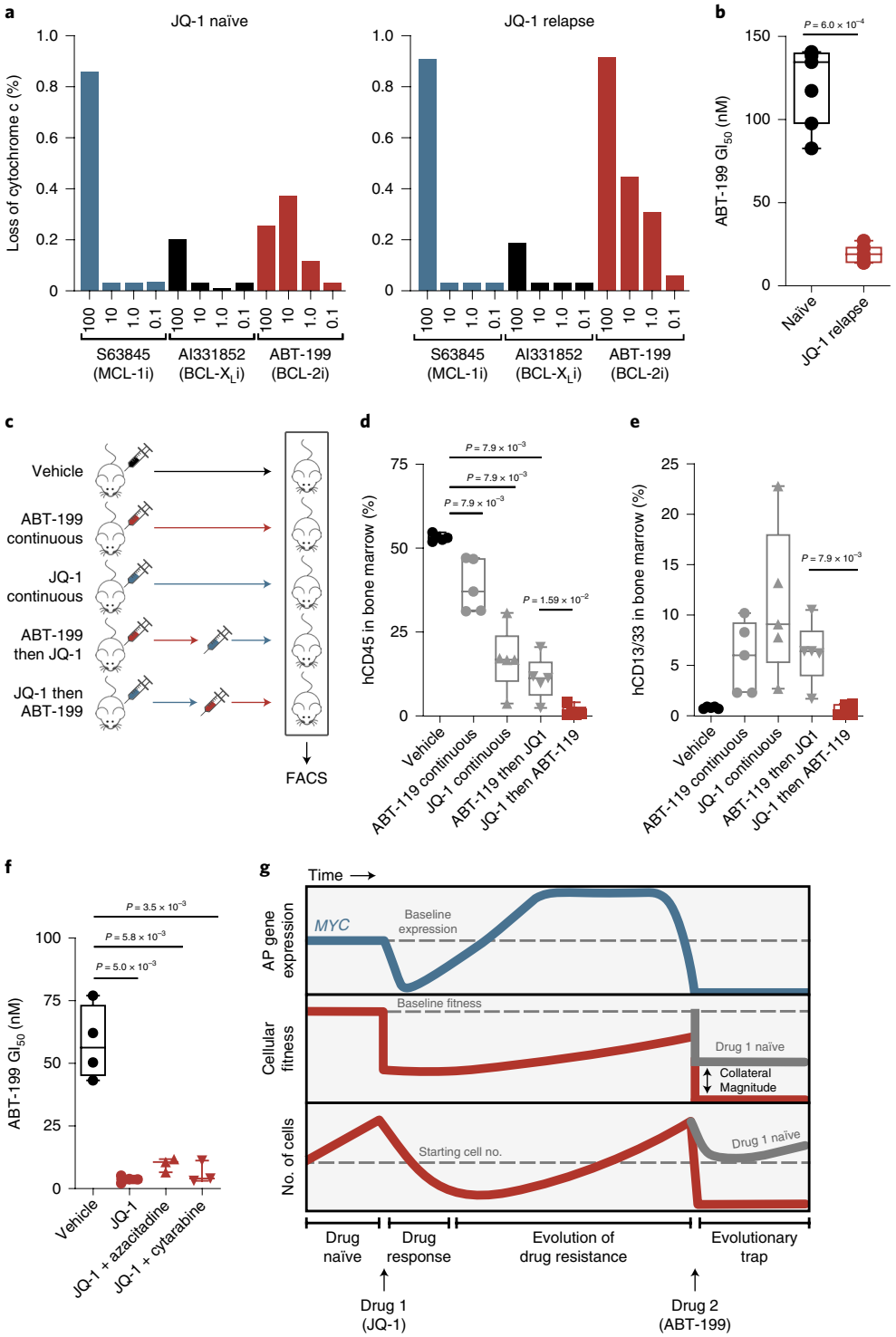

Fig. 5 | JQ-1 treatment primes PDX model of AML for treatment with ABT-199. a, Release of cytochrome *c* upon drug stimulation in JQ-1-naïve and JQ-1-relapsed (50 mg kg^{-1}, intraperitoneal injection) AML PDX cells. **b**, ABT-199 GI_{50} values from JQ-1-naïve and JQ-1-relapsed AML PDX cells. Significance determined by two-tailed Mann–Whitney *U*-test for $n = 5$ biologically independent animals. **c**, Schematic depicting drug-scheduling study in murine PDX model of AML treated with JQ-1 (50 mg kg^{-1}, intraperitoneal injection) and/or ABT-199 (100 mg kg^{-1}, oral gavage) according to indicated drug schedules. **d**,**e**, FACS quantification of human CD45$^+$ (**d**) and human CD13/33$^+$ (**e**) cells from murine bone marrow aspirates of mice in drug-scheduling study. Significance determined by two-tailed Mann–Whitney *U*-test. Data are presented as mean ± s.e.m. for $n = 4$ biologically independent animals. **f**, ABT-199 GI_{50} values in AML PDX cells from treatment-naïve versus mice with relapsed disease following treatment with JQ-1 alone or in combination with cytarabine (5 mg kg^{-1}, intraperitoneal injection) and azacitidine (150 mg kg^{-1}, intraperitoneal injection). Significance determined by two-tailed Mann–Whitney *U*-test for $n = 3$ biologically independent animals. **g**, Proposed model for a chemotherapy-induced evolutionary trap. Treatment of AML cells with JQ-1 prompts compensatory upregulation of *MYC*, an AP gene that harbors proapoptotic potential. Subsequent treatment with ABT-199 produces a potentiated apoptotic response. **b**,**d**–**f**, Box plot elements defined in the Methods.

also exhibit a heightened in vivo response to ABT-199. Moreover, because evolutionary traps do not necessarily work in reverse, and according to our in vitro data we did not expect mice treated with ABT-199 followed by JQ-1 to respond as well, in theory the order of treatment matters. To test these concepts, we performed a drug-switching study where mice engrafted with the PDX were treated with either JQ-1 or ABT-199 for 10 d, after which half of the mice treated with JQ-1 were switched to ABT-199, and vice versa (Fig. 5c). Analysis of bone marrow aspirates showed that mice treated with JQ-1 followed by ABT-199 exhibited lower human CD45$^+$ leukemic infiltration than other groups (Fig. 5d and Extended Data Fig. 9q). Flow cytometry analysis of the myeloid markers CD13 and CD33 indicated that, unlike cells from the other treatment groups, AML cells from mice treated with the progression of JQ-1 to ABT-199 did not exhibit evidence of differentiation, suggesting that the mechanism of blast reduction in these mice was induction of cell death, which is consistent with hypersensitivity to ABT-199-induced apoptosis (Fig. 5e and Extended Data Fig. 9g).

Lastly, chemotherapies that fail to perform as monotherapies frequently gain approval as part of combination regimens[57–59]. This led us to consider whether combination regimens that include JQ-1 could prime AML cells in the same way that JQ-1 monotherapy does. To test this, we treated xenotransplanted mice with JQ-1 combined with cytarabine or azacitidine, chemotherapies that are routinely used to treat AML. Upon disease relapse, engrafted PDX cells were isolated and tested for sensitivity to ABT-199. We observed that, similarly to PDX cells treated with JQ-1 alone, PDX cells treated with combinations that included JQ-1 were sensitized to ABT-199 (Fig. 5f). This result indicates that chemotherapeutic traps can be set with combination therapies, broadening the translatability of this approach.

Discussion

Here, we define a mechanistically coherent chemotherapeutic model that turns the expected acquisition of resistance to an initial drug treatment into an evolutionary trap, setting up a second, more powerful selection event. We designed this trap using genetic screens coupled with the concept of drug-induced AP. This framework enables the rational design of evolutionary traps by connecting the specific mechanisms that drive resistance to an initial drug treatment to their resultant collateral sensitivities (Fig. 5g).

Present circumstances favor the adoption of the principles described here. The majority of modern chemotherapeutic regimens require multiple drugs, often administered sequentially to avoid dose-limiting toxicities. Few of those regimens are molecularly grounded, and they could be restructured to incorporate evolutionary traps, thereby taking advantage of drug-induced AP relationships without drastically changing the status quo. Take, for instance, ABT-199 (venetoclax), which was recently approved by the FDA in combination with cytarabine or a hypomethylating agent for the treatment of AML. Our work suggests that an additional role of venetoclax in the management of AML may be as a second chemotherapy, used to spring a MYC-dependent evolutionary trap in a drug-resistant tumor, especially because many drug-resistance mechanisms in AML appear to feature upregulation of MYC[51,52] or downregulation of EZH2 (ref. [38]). Furthermore, the development of inhibitors of MCL-1 (refs. [37,60]) and BCL-X_L (ref. [61]), which comprise the antiapoptotic defense in many solid tumors[62], suggest that BH3 mimetics could be used to trigger MYC-dependent traps beyond AML, which is an important concept given the prevalence of MYC upregulation in drug-resistant tumors across lineages. With respect to the specific progression of JQ-1 to ABT-199, several bromodomain inhibitors are in clinical trials in AML[63–65]. Our data indicate that patients who relapse on, or are refractory to, treatment with bromodomain inhibitors could be candidates for venetoclax treatment. It is worth mentioning that the up-front combination of bromodomain inhibition and BCL-2 inhibition has also been reported[66,67]. The potency of this combination could be accounted for by our model, through simultaneous eradication of MYC-high and MYC-low cell populations, but the synergy most likely stems from the bromodomain inhibition-induced downregulation of MCL-1 and BCL-X_L.

The ideas explored here motivate several key directions for future study. First, this work focuses on validating an exemplar AP interaction as the substrate for an evolutionary trap. However, the results of our screens performed in the presence of diverse chemotherapies identify a rich landscape of interconnected, drug-induced AP relationships. We expect that further analyses, performed on this or similar chemical genetics datasets, will uncover additional interactions that can be used to design mechanism-based evolutionary traps. Second, the study of AP in evolutionary biology tends to lack formalism. As a result, a majority of AP studies simply identify AP, rather than quantifying it. By establishing the API model that quantifies the relative frequency with which a given gene is observed as having AP, we provide a means for prioritizing AP genes that can be adapted for other studies. Finally, the study of AP in cancer has been limited to only a small number of genes that display context-dependent oncogenic or tumor-suppressive characteristics. A comprehensive, systems-level identification and stratification of AP genes in cancer, driven by application of the quantitative AP model presented here to existing and emerging structural or functional genomic datasets obtained from diverse tumors and cell lines, should allow us to begin to challenge preconceived notions of gene function and essentiality in cancer.

In summary, our work describes how an understanding of the fitness trade-offs inherent to drug-induced AP relationships, mapped through CRISPR–Cas9 loss-of-function screens, can be used to lay an evolutionary trap for cancer. This trap preys on genetic weaknesses exposed in the acquisition of drug resistance, channeling the very mechanism(s) of treatment failure into a second, more powerful selection event. The concepts explored here are valuable, in part because they directly motivate the design of evolutionarily rational chemotherapeutic traps, but more broadly because they have the potential to reframe our understanding of how fundamental evolutionary principles relate to chemotherapeutic responses.

Online content

Any methods, additional references, Nature Research reporting summaries, source data, extended data, supplementary information, acknowledgements, peer review information; details of author contributions and competing interests; and statements of data and code availability are available at https://doi.org/10.1038/s41588-020-0590-9.

Received: 14 May 2019; Accepted: 11 February 2020;
Published online: 16 March 2020

References

1. Kawecki, T. J. & Ebert, D. Conceptual issues in local adaptation. *Ecol. Lett.* **7**, 1225–1241 (2004).
2. Singer, M. C. & Parmesan, C. Lethal trap created by adaptive evolutionary response to an exotic resource. *Nature* **557**, 238–241 (2018).
3. Schlaepfer, M. A., Runge, M. C. & Sherman, P. W. Ecological and evolutionary traps. *Trends Ecol. Evol.* **17**, 474–480 (2002).
4. Robertson, B. A., Rehage, J. S. & Sih, A. Ecological novelty and the emergence of evolutionary traps. *Trends Ecol. Evol.* **28**, 552–560 (2013).
5. Walther, V. et al. Can oncology recapitulate paleontology? Lessons from species extinctions. *Nat. Rev. Clin. Oncol.* **12**, 273–285 (2015).
6. Van Allen, E. M. et al. The genetic landscape of clinical resistance to RAF inhibition in metastatic melanoma. *Cancer Discov.* **4**, 94–109 (2014).
7. Singleton, K. R. et al. Melanoma therapeutic strategies that select against resistance by exploiting MYC-driven evolutionary convergence. *Cell Rep.* **21**, 2796–2812 (2017).
8. Holohan, C. et al. Cancer drug resistance: an evolving paradigm. *Nat. Rev. Cancer* **13**, 714–726 (2013).

9. Gatenby, R. & Brown, J. The evolution and ecology of resistance in cancer therapy. *Cold Spring Harb. Perspect. Med.* **8**, 3 (2018).
10. Konieczkowski, D. J., Johannessen, C. M. & Garraway, L. A. A convergence-based framework for cancer drug resistance. *Cancer Cell* **33**, 801–815 (2018).
11. Gundem, G. et al. The evolutionary history of lethal metastatic prostate cancer. *Nature* **520**, 353–357 (2015).
12. Juric, D. et al. Convergent loss of PTEN leads to clinical resistance to a PI(3) Kα inhibitor. *Nature* **518**, 240–244 (2015).
13. Wang, L. et al. An acquired vulnerability of drug-resistant melanoma with therapeutic potential. *Cell* **173**, 1413–1425.e14 (2018).
14. Chen, G. et al. Targeting the adaptability of heterogeneous aneuploids. *Cell* **160**, 771–784 (2015).
15. Imamovic, L. et al. Drug-driven phenotypic convergence supports rational treatment strategies of chronic infections. *Cell* **172**, 121–134.e14 (2018).
16. Amirouchene-Angelozzi, N., Swanton, C. & Bardelli, A. Tumor evolution as a therapeutic target. *Cancer Discov.* **7**, 805–817 (2017).
17. Zhao, B. et al. Exploiting temporal collateral sensitivity in tumor clonal evolution. *Cell* **165**, 234–246 (2016).
18. Savolainen, O., Lascoux, M. & Merila, J. Ecological genomics of local adaptation. *Nat. Rev. Genet.* **14**, 807–820 (2013).
19. Tiffin, P. & Ross-Ibarra, J. Advances and limits of using population genetics to understand local adaptation. *Trends Ecol. Evol.* **29**, 673–680 (2014).
20. Hart, T. et al. Measuring error rates in genomic perturbation screens: gold standards for human functional genomics. *Mol. Syst. Biol.* **10**, 733 (2014).
21. Shalem, O. et al. Genome-scale CRISPR–Cas9 knockout screening in human cells. *Science* **343**, 84–87 (2014).
22. Lin, K. H. et al. Systematic Dissection of the Metabolic-Apoptotic Interface in AML Reveals Heme Biosynthesis to Be a Regulator of Drug Sensitivity. *Cell Metab.* **29**, 1217–1231.e7 (2019).
23. Fiskus, W. et al. Highly effective combination of LSD1 (KDM1A) antagonist and pan-histone deacetylase inhibitor against human AML cells. *Leukemia* **28**, 2155–2164 (2014).
24. Fiskus, W. et al. Combined epigenetic therapy with the histone methyltransferase EZH2 inhibitor 3-deazaneplanocin A and the histone deacetylase inhibitor panobinostat against human AML cells. *Blood* **114**, 2733–2743 (2009).
25. Beaumont, K. A. et al. Cell cycle phase-specific drug resistance as an escape mechanism of melanoma cells. *J. Invest. Dermatol.* **136**, 1479–1489 (2016).
26. Knutson, S. K. et al. Synergistic anti-tumor activity of EZH2 inhibitors and glucocorticoid receptor agonists in models of germinal center non-Hodgkin lymphomas. *PLoS ONE* **9**, e111840 (2014).
27. Lee, T., Karon, M. & Momparler, R. L. Kinetic studies on phosphorylation of 5-azacytidine with the purified uridine-cytidine kinase from calf thymus. *Cancer Res.* **34**, 2482–2488 (1974).
28. Liliemark, J. O., Plunkett, W. & Dixon, D. O. Relationship of 1-β-D-arabinofuranosylcytosine in plasma to 1-β-D-arabinofuranosylcytosine 5′-triphosphate levels in leukemic cells during treatment with high-dose 1-β-D-arabinofuranosylcytosine. *Cancer Res.* **45**, 5952–5957 (1985).
29. Cai, J. et al. Two distinct molecular mechanisms underlying cytarabine resistance in human leukemic cells. *Cancer Res.* **68**, 2349–2357 (2008).
30. Margueron, R. & Reinberg, D. The Polycomb complex PRC2 and its mark in life. *Nature* **469**, 343–349 (2011).
31. Holoch, D. & Margueron, R. Mechanisms regulating PRC2 recruitment and enzymatic activity. *Trends Biochem. Sci.* **42**, 531–542 (2017).
32. Schmitges, F. W. et al. Histone methylation by PRC2 is inhibited by active chromatin marks. *Mol Cell* **42**, 330–341 (2011).
33. Zheng, Y. et al. Total kinetic analysis reveals how combinatorial methylation patterns are established on lysines 27 and 36 of histone H3. *Proc. Natl Acad. Sci. USA* **109**, 13549–13554 (2012).
34. Bennett, R. L. et al. The role of nuclear receptor-binding SET domain family histone lysine methyltransferases in cancer. *Cold Spring Harb. Perspect. Med.* **7**, a026708 (2017).
35. Kaur, M. & Cole, M. D. MYC acts via the PTEN tumor suppressor to elicit autoregulation and genome-wide gene repression by activation of the Ezh2 methyltransferase. *Cancer Res.* **73**, 695–705 (2013).
36. Lin, K. H. et al. Targeting MCL-1/BCL-XL forestalls the acquisition of resistance to ABT-199 in acute myeloid leukemia. *Sci. Rep.* **6**, 27696 (2016).
37. Ramsey, H. E. et al. A novel MCL1 inhibitor combined with venetoclax rescues venetoclax-resistant acute myelogenous leukemia. *Cancer Discov.* **8**, 1566–1581 (2018).
38. Gollner, S. et al. Loss of the histone methyltransferase EZH2 induces resistance to multiple drugs in acute myeloid leukemia. *Nat. Med.* **23**, 69–78 (2017).
39. Farrell, A. S. & Sears, R. C. MYC degradation. *Cold Spring Harb. Perspect. Med.* **4**, a014365 (2014).
40. Bradley, W. D. et al. EZH2 inhibitor efficacy in non-Hodgkin's lymphoma does not require suppression of H3K27 monomethylation. *Chem. Biol.* **21**, 1463–1475 (2014).
41. Ryan, J. & Letai, A. BH3 profiling in whole cells by fluorimeter or FACS. *Methods* **61**, 156–164 (2013).
42. Campone, M. et al. c-Myc dependent expression of pro-apoptotic Bim renders HER2-overexpressing breast cancer cells dependent on anti-apoptotic Mcl-1. *Mol. Cancer* **10**, 110 (2011).
43. Lee, Y. Y. et al. CREB-binding protein (CBP) regulates β-adrenoceptor (β-AR)-mediated apoptosis. *Cell Death Differ.* **20**, 941–952 (2013).
44. Muthalagu, N. et al. BIM is the primary mediator of MYC-induced apoptosis in multiple solid tissues. *Cell Rep.* **8**, 1347–1353 (2014).
45. Villunger, A. et al. p53- and drug-induced apoptotic responses mediated by BH3-only proteins puma and noxa. *Science* **302**, 1036–1038 (2003).
46. Nakano, K. & Vousden, K. H. PUMA, a novel proapoptotic gene, is induced by p53. *Mol. Cell* **7**, 683–694 (2001).
47. Ni Chonghaile, T. et al. Pretreatment mitochondrial priming correlates with clinical response to cytotoxic chemotherapy. *Science* **334**, 1129–1133 (2011).
48. Dauch, D. et al. A MYC-aurora kinase A protein complex represents an actionable drug target in p53-altered liver cancer. *Nat. Med.* **22**, 744–753 (2016).
49. Stine, Z. E. et al. MYC, metabolism, and cancer. *Cancer Discov.* **5**, 1024–1039 (2015).
50. den Hollander, J. et al. Aurora kinases A and B are up-regulated by Myc and are essential for maintenance of the malignant state. *Blood* **116**, 1498–1505 (2010).
51. Fong, C. Y. et al. BET inhibitor resistance emerges from leukaemia stem cells. *Nature* **525**, 538–542 (2015).
52. Rathert, P. et al. Transcriptional plasticity promotes primary and acquired resistance to BET inhibition. *Nature* **525**, 543–547 (2015).
53. Shu, S. et al. Response and resistance to BET bromodomain inhibitors in triple-negative breast cancer. *Nature* **529**, 413–417 (2016).
54. Xia, B. et al. c-Myc plays part in drug resistance mediated by bone marrow stromal cells in acute myeloid leukemia. *Leuk. Res.* **39**, 92–99 (2015).
55. Zhang, Y. et al. Sp1 and c-Myc modulate drug resistance of leukemia stem cells by regulating survivin expression through the ERK-MSK MAPK signaling pathway. *Mol. Cancer* **14**, 56 (2015).
56. Pan, X. N. et al. Inhibition of c-Myc overcomes cytotoxic drug resistance in acute myeloid leukemia cells by promoting differentiation. *PLoS ONE* **9**, e105381 (2014).
57. Cortes, J. E. et al. Glasdegib plus intensive/nonintensive chemotherapy in untreated acute myeloid leukemia: BRIGHT AML 1019 Phase III trials. *Future Oncol.* **15**, 3531–3545 (2019).
58. Cortes, J. E. et al. Randomized comparison of low dose cytarabine with or without glasdegib in patients with newly diagnosed acute myeloid leukemia or high-risk myelodysplastic syndrome. *Leukemia* **33**, 379–389 (2019).
59. DiNardo, C. D. et al. Venetoclax combined with decitabine or azacitidine in treatment-naive, elderly patients with acute myeloid leukemia. *Blood* **133**, 7–17 (2019).
60. Kotschy, A. et al. The MCL1 inhibitor S63845 is tolerable and effective in diverse cancer models. *Nature* **538**, 477–482 (2016).
61. Leverson, J. D. et al. Exploiting selective BCL-2 family inhibitors to dissect cell survival dependencies and define improved strategies for cancer therapy. *Sci. Transl. Med.* **7**, 279ra40 (2015).
62. Soderquist, R. S. et al. Systematic mapping of BCL-2 gene dependencies in cancer reveals molecular determinants of BH3 mimetic sensitivity. *Nat. Commun.* **9**, 3513 (2018).
63. Xu, Y. & Vakoc, C. R. Targeting cancer cells with BET bromodomain inhibitors. *Cold Spring Harb. Perspect. Med.* **7**, a026674 (2017).
64. Stathis, A. & Bertoni, F. BET proteins as targets for anticancer treatment. *Cancer Discov.* **8**, 24–36 (2018).
65. Berthon, C. et al. Bromodomain inhibitor OTX015 in patients with acute leukaemia: a dose-escalation, phase 1 study. *Lancet Haematol.* **3**, e186–e195 (2016).
66. Fiskus, W. et al. Superior efficacy of cotreatment with BET protein inhibitor and BCL2 or MCL1 inhibitor against AML blast progenitor cells. *Blood Cancer J.* **9**, 4 (2019).
67. Esteve-Arenys, A. et al. The BET bromodomain inhibitor CPI203 overcomes resistance to ABT-199 (venetoclax) by downregulation of BFL-1/A1 in in vitro and in vivo models of MYC+/BCL2+ double hit lymphoma. *Oncogene* **37**, 1830–1844 (2018).

Methods

Cell lines and reagents. All cell lines were maintained in a humidified incubator at 37 °C with 5% CO_2. HCC827, KM-12, PC9, MOLM-13, OCI-AML2, MV4;11, KG-1a, HL-60 and UACC-62 cells were cultured in RPMI 1640 medium with 10% fetal bovine serum (FBS) and 1% penicillin–streptomycin. OCI-AML2, MOLM-13 and MV4;11 have wild-type p53, while HL-60 and KG-1a have mutated p53. SKMEL5 cells were cultured in DMEM with 10% FBS and 1% penicillin–streptomycin. 293FT cells were cultured in DMEM high glucose medium with 10% FBS, 1% penicillin–streptomycin, 1% sodium pyruvate, 1% nonessential amino acids and 1% GlutaMax. All cell lines were purchased from American Type Culture Collection or Duke University Cell Culture Facility. Drugs were purchased from ApexBio (S63485), Cayman Chemical (WEHI-539), ARV771 (MedChem) and SelleckChem (all other inhibitors).

Evolving drug-resistant cell lines. To achieve drug resistance in vitro, AML cells were continuously cultured in increasing concentrations of drug. Cells were first drugged at a dose approximately equal to their GI_{50} value (concentration for 50% of maximal inhibition of cell proliferation). The growth rate was monitored with weekly passaging and the concentration of drug was increased once a stable growth rate was achieved. Solid tumor cell lines were evolved to resistance either as described above or by treating cells with a high drug concentration and selecting resistant clones.

The maximally tolerated dose of JQ-1 corresponding to each resistant cell line was as follows: OCI-AML2 (250 nM), MV4;11 (150 nM), MOLM-13 (200 nM), KG-1a (250 nM) and HL-60 (200 nM). These doses were achieved gradually over the course of 2 months.

Short-term cell viability assay (GI_{50}). AML cells were seeded into 96-well plates at a density of 7,500 cells per well. Immediately following plating, AML cells were treated with vehicle (DMSO) or a tenfold serial dilution of drug. Each treatment condition was conducted in triplicate. Solid tumor cells were plated at a density of 2,000 cells per well and treated after 24 h. Three days following addition of drug, cell viability was quantified using Cell Titer Glo (Promega). The relative cell viability was determined by normalizing the raw luminescence values for each treatment condition to DMSO-treated wells. For experiments involving two drugs, slight modifications were made. One drug was kept at a constant concentration across all wells and a serial dilution of a second drug was added on top of the background drug. One well was treated with DMSO only and one well was treated with background drug only. The relative cell viability was normalized to the luminescence of the background drug only. Dose–response curves were fit using GraphPad/Prism 7/8 software. GI_{50} values were interpolated from the resultant graphs as the dose corresponding to 50% cell viability relative to DMSO-treated cells.

Cloning CRISPR library. Our CRISPR library was cloned according to previously described methods[21]. Each gene in the library was represented by five sgRNAs, pulled from a previously published, full-genome CRISPR library[68]. Also included were 50 nontargeting controls. In brief, each unique 20-mer sgRNA sequence was appended by constant prefix and suffix sequences (Supplementary Table 5) and synthesized as an oligonucleotide pool by Custom Array. The pooled inserts were diluted 1:10 in molecular-grade water and amplified with NEB Phusion Hotstart Flex enzyme mix using the following primers:

Array_Forward: see Supplementary Table 5.

Array_Reverse: see Supplementary Table 5.

Protocol: 98 °C (30 s), 18× (98 °C (10 s), 63 °C (10 s), 72 °C (15 s)), 72 °C (3 min).

Double-stranded inserts were cleaned up with Axygen magnetic PCR bead purification kits (Fisher Scientific) and eluted in molecular-grade water. lentiCRISPRv2 (Addgene, plasmid no. 52961) was digested with FastDigest BsmBI at 37 °C for 2 h and the cut vector was gel extracted. A 20-µl Gibson assembly reaction was performed using 100 ng of cut lentiCRISPRv2 and 40 ng of prepped sgRNA inserts. The Gibson reaction product (1 µl) was transformed into electrocompetent cells (E. cloni 10G ELITE, Lucigen, catalog no. 60052-2) and spread onto LB-ampicillin plates. Following overnight incubation at 37 °C, plates were counted to ensure 40× library coverage, colonies were scraped and plasmid DNA was isolated using a Maxiprep kit (Qiagen). Fifty colonies were individually cultured and sequenced to validate cloning fidelity.

Individual sgRNA oligonucleotides were prepared, cleaned up, cloned, transformed, isolated and validated in an analogous manner.

pCDH-puro-cMyc was a gift from J. Wang (Addgene, plasmid no. 46970).

Lentivirus production. Lentivirus production was conducted as previously described[22], with slight modification. Briefly, 293FT cells were grown to 60–70% confluency and transfected using Fugene6 (Promega), 2.80 µg of psPAX2, 0.280 µg of pVSVg and 2.80 µg of plasmid. After 30 min of incubation at room temperature, the transfection mixture was added dropwise to 293FT. After 24 h, medium was aspirated and replaced with collection medium (DMEM with 30% FBS, 1% penicillin–streptomycin). After 48 h, the virus was collected, cleared through 5-min centrifugation at 1,200 r.p.m. and passed through a 0.45-µm filter to remove cell particles. Viral titers and transductions were performed as previously described[22].

Pooled CRISPR screening. OCI-AML2 cells were seeded into 6-well plates at a density of 3×10^6 cells per well and transduced at a multiplicity of infection of 0.2. A total of 144×10^6 cells were transduced in 48 wells. At 24 h after viral transduction, cells were replated into puromycin-containing medium. A sample was collected at 48 h of puromycin exposure to confirm library coverage in the transduced population. Transduced cells were expanded in puromycin for a total of 10 d before drug introduction, at which point the transduced cell population was split into vehicle (DMSO) and drug-treatment conditions and maintained for 2 weeks. All conditions were performed in replicate. Drugs were used at doses sufficient to achieve 20–30% loss of viability as follows: 100 nM ABT-199, 100 nM selinexor, 50 nM JQ-1, 1 µM quizartinib, 600 nM vorinostat, 60 nM cytarabine, 2 nM mitoxantrone, 100 nM decitabine and 1 µM azacitidine. Cells were counted, replated and the drug replenished every 3–4 d. At any given point during the screen each replicate was represented by a minimum of 12×10^6 cells, which was sufficient to provide 1,000× coverage of the library (~1,000 cells per unique sgRNA). Samples of 25×10^6 cells were collected upon screen initiation, termination and at weekly intervals. Following completion of the screens, DNA was extracted (DNeasy Blood & Tissue Kit, Qiagen) and prepared for sequencing as previously described[22].

CRISPR screen analysis. Deep sequencing was performed on an Illumina NextSeq platform (75 base pair, single-ended) to identify differences in library composition. All sequencing was performed by Hudson Alpha Institute for Biotechnology. Barcoded reads were matched and binned into guide-level counts. Determinations of genetic essentiality and drug sensitization/resistance were made by evaluating differential guide compositions between the initial population and subsequent drug-treated and vehicle-treated cell populations. Briefly, the fractional representation (FR) for a guide within a sample was normalized to the sum of all guides attributed to that sample. A direct comparison between two samples entailed the quotient of the respective FRs, which we term the depletion metric (DM). The five guide-level DMs for each gene were then collapsed to gene-level scores by taking the average. Guides that totaled fewer than 200 counts for a given sample were excluded from the analysis. Genetic essentiality was calculated by considering the depletion/enrichment of the vehicle-treated population over time ($DMSO_{final}/DMSO_{initial}$). Drug sensitization/resistance was calculated by considering the depletion/enrichment of the drug-treated population relative to the vehicle-treated population ($Drug_{final}/DMSO_{final}$). All depletion/enrichment effects are reported as $\log_2$ ratios. All described manipulations were performed in R.

Identification of AP genes. To establish a framework for the systematic identification of AP genes, we accepted the following definition of an AP gene: a gene whose null allele (here achieved through CRISPR–Cas9-mediated genetic ablation) confers relative fitness under one condition and relative loss of fitness under another condition. This definition permits flexibility at two points: the (number and type of) conditions observed, and the relative threshold for defining gain or loss of fitness. The identified AP genes in a given analysis are a function of these variables. As the number of conditions approaches infinity, the number of AP genes identified approaches the total number of genes monitored. Our examination of a nine-drug chemotherapy panel does not exhaust, but approaches saturation of, our 2,390-gene library. Second, the definition of an observed effect on relative fitness is necessarily measured against a fitness threshold. As the fitness threshold approaches zero (null effect), the number of AP genes identified approaches the total number of genes monitored. The stringency of this threshold dictates both the quantity and the 'quality' of the AP genes identified. Because the absolute depletion/enrichment engendered by drug treatment on top of gene knockout is a function of the dose and duration of drug exposure, an absolute depletion/enrichment cutoff was avoided in favor of a relative cutoff defined by the topology of the curve. In short, a five-gene, moving average of the slope was calculated across the ranked, gene-level scores corresponding to each drug-treated screen. The cutoffs that distinguished fitness loss from inertness from fitness gain were defined as the points where the moving average of the slope first equaled the slope of the middle 50% of the curve (Extended Data Fig. 2a). Each cutoff was evaluated against the distribution of nontargeting control genes (outliers excluded by Tukey's rule) and controlled at $P<0.05$. Complete sets of fitness-beneficial and fitness-detrimental genes were compiled by identifying the genes that score above (fitness-beneficial) and below (fitness-detrimental) both topological and statistical cutoffs in at least one condition. The intersection of those two gene sets yielded the full set of AP genes.

Calculation of API. See Supplementary Note.

Circos plot. The circos plots shown in Fig. 2a and Extended Data Fig. 2c were assembled using Circos (http://circos.ca/).

Clustered heat maps. Heat maps were produced in R with the gplots package. Unsupervised clustering was performed from the Euclidean distance matrix according to Ward's clustering criterion.

Correlogram. Correlograms shown in Extended Data Figs. 2f and 3a,j were assembled by first calculating correlations between relevant AP genes across all conditions screened. Correlograms were produced in R with the corrplot package.

Gene ontology analysis. Gene ontology of extrinsic AP genes was performed using the GeneOntology biological process platform (http://geneontology.org). Default gene ontology terms were included in the analysis.

qRT–PCR. RNA was isolated from whole cells with QIAshredder Homogenizers and the RNEasy Mini kit (Qiagen). Complementary DNA was reverse transcribed from total RNA samples using the iScript cDNA Synthesis Kit with 1 µg of RNA template. qRT–PCR was carried out using iQ SYBR Green Supermix and a CFX384 Touch Real-Time PCR Detection System, according to the manufacturer's instructions. Fold expression was determined by normalizing cycle threshold (C_q) values to the *ACTB* reference gene and normalizing samples to the control sample, in accordance with the $\Delta\Delta C_q$ method.

For primers, see Supplementary Table 5.

Western blot. *Immunoblotting.* Immunoblotting was performed as previously described[22], with slight modification. Protein lysates were prepared with RIPA lysis buffer supplemented with 1× protease inhibitor cocktail. Crude lysates were cleared using QIAshredder Homogenizers (Qiagen) and centrifuged at 13,000 r.p.m. for 2 min at 4 °C. Membranes were probed with primary antibodies β-actin (Cell Signaling Technology (CST) no. 4970, CST no. 5453 diluted 1:3,000 in 5% BSA), Myc (Y69) (Abcam, ab32072), Ezh2 (D2C9) (CST no. 5246 diluted 1:1,000 in 5% BSA), acetyl-histone H3 (Lys27) (CST no. 8173, CST no. 5453 diluted 1:1,000 in 5% BSA), Bim (CST no. 2933 diluted 1:500 in 5% BSA), Puma (CST no. 12450 diluted 1:500 in 5% BSA), Noxa (CST no. 14766 diluted 1:500 in 5% BSA), Bcl-2 (CST no. 4223, CST no. 5453 diluted 1:1,000 in 5% BSA), Mcl-1 (CST no. 5453 diluted 1:1,000 in 5% BSA), Bcl-x_L (CST no. 2764), Nsd2 (Abcam, ab75359 diluted 1:500 in 5% BSA), Nsd3 (Abcam, ab4514 diluted 1:500 in 5% BSA), LSD1 (CST no. 2139 diluted 1:1,000 in 5% BSA), H3K4me1 (Abcam, ab8895 diluted 1:2,000 in 5% BSA) and H3K9me2 (CST no. 4658 diluted 1:1,000 in 5% BSA) overnight (16 h). Following incubation with HRP-conjugated secondary antibody, blots were developed with SuperSignal West Pico PLUS Chemiluminescent Substrate (ThermoFisher) or ECL Western Blotting Substrate (ThermoFisher). All uncropped images have been provided as source data.

Immunoprecipitation. For coimmunoprecipitation cells were resuspended in lysis buffer (50 mM Tris–HCl pH 7.4, 150 mM NaCl, 20 mM EDTA, 50 mM NaF, 0.5% NP-40, 1 mM dithiothreitol with EDTA-free protease inhibitor and PhosSTOP phosphatase inhibitor tablets), rotated for 1 h at 4 °C and cleared by centrifugation at 14,000 r.p.m. for 20 min at 4 °C. Lysates were then equilibrated to 500 µg of protein in 1 ml lysis buffer and acquainted with 50 µl protein G-Sepharose (Invitrogen) preincubated with 1:100 dilution of anti-EZH2 primary antibody (CST no. 5246) and rotated overnight at 4 °C. Samples were washed five times with lysis buffer, boiled for 5 min, loaded into sample buffer and run on the gel.

Cycloheximide chase. Parental and resistant AML cells were treated with cycloheximide (CST, catalog no. 2112, 20 µg ml^{-1} in DMSO) for the indicated times. Cells were collected and subjected to western blot analysis to assess MYC stability following inhibition of protein synthesis. Immunoblots were quantified using ImageJ v.1.51S software.

Flow cytometry. Live cells (1.5×10^6 cells per sample) were washed with PBS then with FACS buffer (PBS with 2% FBS, 2 mM EDTA and 0.9% sodium azide) before staining with CD11b-PE antibody (BioLegend, catalog no. 101207, diluted 1:500 in FACS buffer) for 30 min at 4 °C and subjected to cytometric analysis with a BD FACSCanto II.

BH3 profiling. BH3 profiling was performed as described previously[69]. In short, parental and JQ-1-resistant OCI-AML2 cells were collected, washed with PBS and resuspended in Newmeyer buffer followed by permeabilization with digitonin. Samples were exposed to BH3 peptides and monitored for mitochondrial transmembrane potential loss using JC-1. Measurements were taken at 590 nM at 30 °C every 5 min for 3 h.

Cytochrome *c* loss assay. Cytochrome *c* loss assay was performed as described previously[70]. Cells (5.0×10^6) were washed in PBS, then stained with Zombie Aqua Fixable Viability dye (BioLegend) and anti-CD45 APC H7 (BD Biosciences, clone 2D1). Cells were resuspended in DTEB buffer and permeabilized with digitonin. Cells (200×10^3) were incubated with different concentrations (100, 10, 1 and 0.1 µM) of S63845, AI331852 and ABT-199 for 1 h. Cells were then fixated with 8% formaldehyde. After fixation termination with N2 buffer, cells were labeled with anti-human cytochrome *c* (CytC) Alexa Fluor 488 (BD Biosciences, clone 6H2.B4). All experiments included two DMSO 2% samples (without BH3 mimetics peptide), one labeled with anti-cytochrome *c* and one unlabeled, as positive and negative controls for mitochondrial cytochrome *c* content, respectively. Flow cytometry analysis was then performed on a BD Fortessa analyzer (BD Biosciences).

In vivo transplantation. The French National Committee on Animal Care reviewed and approved all mouse experiments described in this study. Primary patient AML blasts were collected from bone marrow aspirates after obtaining informed patient consent under a St Louis Hospital Internal Review Board approved protocol. Mononuclear cells were isolated using Ficoll-Paque Plus (Amersham Biosciences) and red blood cells were lysed before flow cytometry analysis. These cells were maintained in StemSpan SFEM (StemCell Technologies, catalog no. 09650) medium supplemented with 20 ng ml^{-1} IL-3 (Peprotech, catalog no. 200–03), 20 ng ml^{-1} IL-6 (Peprotech, catalog no. 200-06), 20 ng ml^{-1} GM-CSF (Peprotech, catalog no. 300-03), 100 ng ml^{-1} FLT3-ligand (Peprotech, catalog no. 300-19) and 100 ng ml^{-1} SCF (Peprotech, catalog no. 300-07) before injection into NOD.Cg-Prkdcscid Il2rgtm1Sug Tg(SV40/HTLV-IL-3,CSF2)10-7Jic/JicTac (huNOG-EXL) mice purchased from Taconic. Sample size was chosen in light of the fact that these in vivo models were historically highly penetrant and consistent. Animals were excluded from the study if any signs of distress were observed without clinical signs of leukemia: that is, absence of leukemic blasts in bone marrow, spleen and blood. None of our animals were excluded on the basis of these criteria. Blinded observers visually inspected mice for obvious signs of distress, such as loss of appetite, hunched posture and lethargy. Approximately 0.65×10^6 cells were tail-vein-injected as a secondary transplant into sublethally irradiated (125 cGy) 6–8-week-old male huNOG-EXL mice.

Drug-scheduling experiments. Twelve days after injection, mice were randomized and treated daily either by oral gavage with 100 mg kg^{-1} ABT-199 (60% Phosal 50 + 30% PEG-400 + 10% ethanol), by intraperitoneal injection with 50 mg kg^{-1} JQ-1 (10% DMSO + 90% G5W) or with these two drugs used consecutively as indicated in the figures. Bone marrow biopsies were performed on anesthetized animals 28 d after cell injection, and biopsies were washed once in PBS and resuspended in 0.5% BSA, 2 mM EDTA–PBS before staining with either APC-conjugated anti-human CD45 (BioLegend, catalog no. 368512, 3:100) or a cocktail of PE-Cy7-conjugated anti-human CD13/33 (eBioscience, catalog no. 25-0138-42 and 25-0338-42, 3:100) antibodies and flow cytometry analysis.

Drug-relapsed experiments. Twelve days after injection, mice were randomized into five groups of four mice each and treated daily either by oral gavage 15 mg kg^{-1} EPZ-6438 (20% Captisol, 7 d), intraperitoneal injection with 50 mg kg^{-1} JQ-1 (10% DMSO + 90% G5W, 7 d), JQ-1 + intraperitoneal injection 5 mg kg^{-1} azacitidine (HBSS, 5 d), JQ-1 + intraperitoneal injection 150 mg kg^{-1} cytarabine (HBSS, 5 d) or vehicle. Upon disease relapse, mice were killed and the whole bone marrow was collected and stained with anti-hCD45 before flow cytometry-based sorting of hCD45-positive AML blasts. ABT-199 GI_{50} values were obtained by plating sorted blasts in 384-well plates in the presence of increasing concentrations of ABT-199 for 3 d (top concentration of 5 µM).

Statistical analyses. All results are shown as mean ± s.e.m. Unless specified, *P* values were determined using unpaired, two-tailed Student's *t*-tests. *P* values <0.05 were considered significant. *P* values are provided as exact values whenever significant. Unless otherwise noted, all measurements were taken from distinct samples. Box plot elements were defined as: box extends from 25th to 75th percentile; whiskers extend from the minimum to maximum value; median indicated by traversing line.

Reporting Summary. Further information on research design is available in the Nature Research Reporting Summary linked to this article.

Data availability

The data supporting the findings of this study are found within the paper and supplementary files. Source Data for Figs. 2–5 and Extended Data Figs. 2 and 4–9 are available online.

Code availability

Scripts for analyzing CRISPR–Cas9 screens and calculating API are available on Github (https://github.com/linkvein/).

References

68. Wang, T. et al. Genetic screens in human cells using the CRISPR–Cas9 system. *Science* **343**, 80–84 (2014).
69. Sarosiek, K. A. et al. BID preferentially activates BAK while BIM preferentially activates BAX, affecting chemotherapy response. *Mol. Cell* **51**, 751–765 (2013).
70. Vo, T. T. et al. Relative mitochondrial priming of myeloblasts and normal HSCs determines chemotherapeutic success in AML. *Cell* **151**, 344–355 (2012).

Acknowledgements

We thank the members of the K.C.W. laboratory and A. Puissant laboratory for helpful discussions and scientific input. We also thank K. Wood (University of Michigan), G. Blobe and S. Floyd (Duke Pharmacology & Cancer Biology) for providing helpful feedback. This work was supported by Duke University School of Medicine start-up funds and support from the Duke Cancer Institute (K.C.W.), NIH awards (R01CA207083

to K.C.W., F30CA206348 to K.H.L. and F31CA195967 to P.S.W.), National Science Foundation Graduate Research Fellowship awards (DGE-1106401 to G.R.A. and DGF-1106401 to L.C.), the Duke Medical Scientist Training Program (T32 GM007171 to K.H.L.), the Duke Undergraduate Research Support Office (to J.C.R. and A.X.), the ATIP/AVENIR French research program (to A.P.) and the EHA research grant for Non-Clinical Advanced Fellow (to A.P.). A.P. is a recipient of support from the ERC Starting program (758848) and supported by the St Louis Association for leukemia research. Any opinions, findings and conclusions or recommendations expressed in this material are those of the authors(s) and do not necessarily reflect the views of the National Science Foundation or the NIH. Finally, we dedicate this work to the memory of our friend, Kimberly Brigati Wang, and her courageous fight against AML.

Author contributions

K.H.L., J.C.R., A.P. and K.C.W. conceptualized the project. K.H.L. and J.C.R. were responsible for methodology. Validation was done by K.H.L. and J.C.R. K.H.L., J.C.R., A.X., Z.D. and E.T.W. performed the formal analysis. The investigation was carried out by K.H.L., J.C.R., A.X., Y.-R.A., B.P., R.D.B., A.F. and R.I. Resources were collected by Y.-R.A., R.T.S., G.R.A., K.R.S., A.E.D., P.S.W., A.P. and K.C.W. Data were curated by K.H.L., J.C.R., A.X. and J.W.L. The original draft was written by K.H.L., J.C.R. and K.C.W. All authors reviewed and edited the paper. K.H.L. and J.C.R. were responsible for visualization. L.C., A.P. and K.C.W. supervised the project. Funding was acquired by K.H.L., G.R.A., P.S.W., A.P. and K.C.W.

Competing interests

J.W.L. serves on the scientific advisory board and owns equity in Nanocare Technologies and Raphael Pharmaceuticals. R.I. has received previous funding from Oncoethix SA for work on the bromodomain inhibitor OTX015. The remaining authors declare no competing interests.

Additional information

Extended data is available for this paper at https://doi.org/10.1038/s41588-020-0590-9.

Supplementary information is available for this paper at https://doi.org/10.1038/s41588-020-0590-9.

Correspondence and requests for materials should be addressed to A.P. or K.C.W.

Reprints and permissions information is available at www.nature.com/reprints.

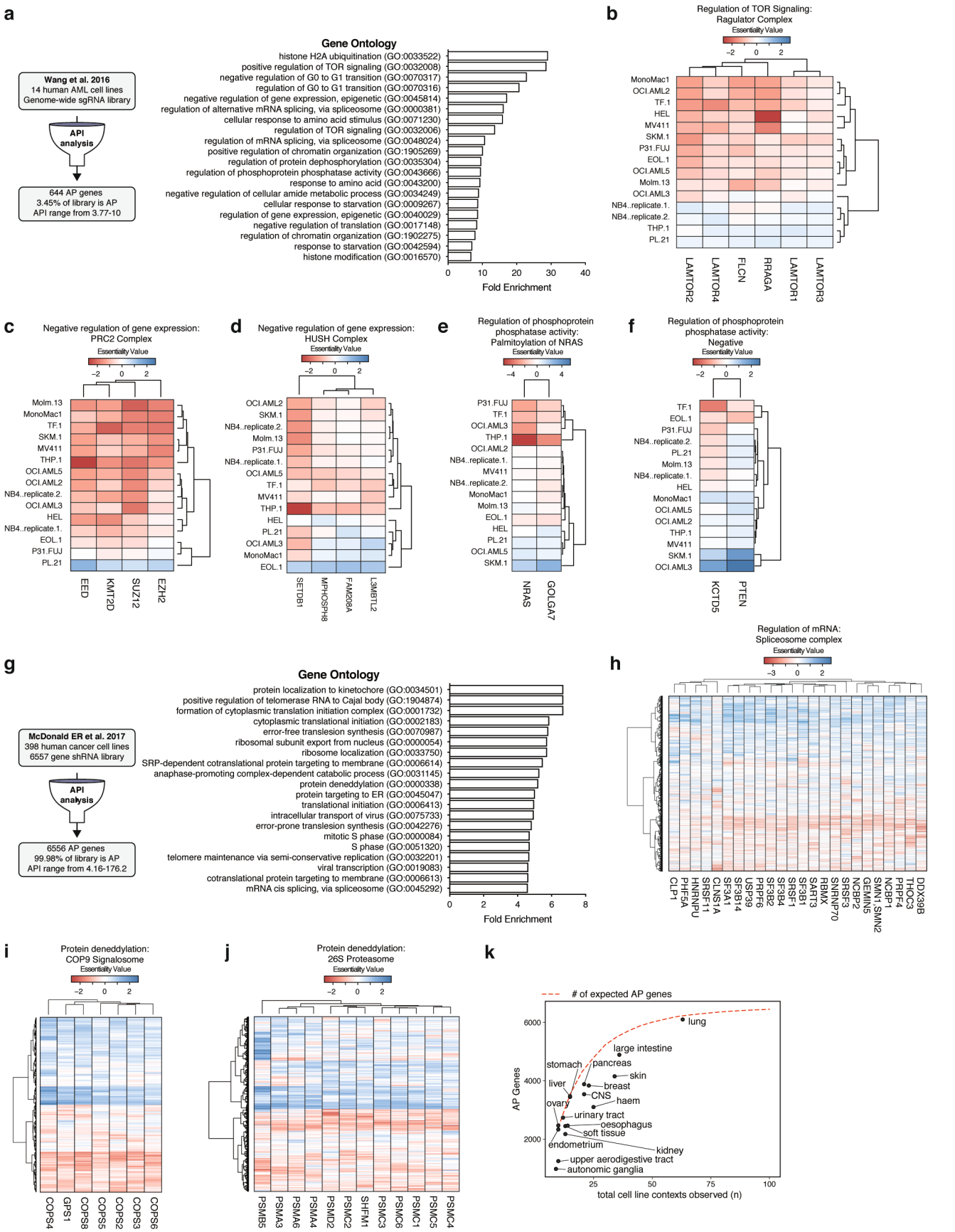

Extended Data Fig. 1 | See next page for caption.

Extended Data Fig. 1 | Validation of API using external datasets. a, API analysis performed on published CRISPR/Cas9-based gene essentiality dataset identifies overrepresented gene ontologies in top 15% of AP genes across 14 AML cell lines. **b–f**, Exemplar gene networks associated with overrepresented gene ontologies in **(a)**. **g**, API analysis performed on published shRNA-based gene essentiality dataset identifies overrepresented gene ontologies in top 15% of AP genes across 398 human cancer cell lines. **h–j**, Exemplar gene networks associated with overrepresented gene ontologies in **(g)**. **k**, Cell line lineages represented in published shRNA-based gene essentiality dataset plotted according to number of AP genes versus number of cell lines within each lineage. Red dashed line depicts number of AP genes with random sampling of cell lines for a given n. **l**, Cell line lineages plotted according to fraction of expected AP, defined as the number of AP genes in a given linage divided by number of expected AP genes for a given n. **b–f**; **h–j**, Heatmaps generated by unsupervised hierarchical clustering of genes (columns) and cell lines (rows) based on Euclidean distance.

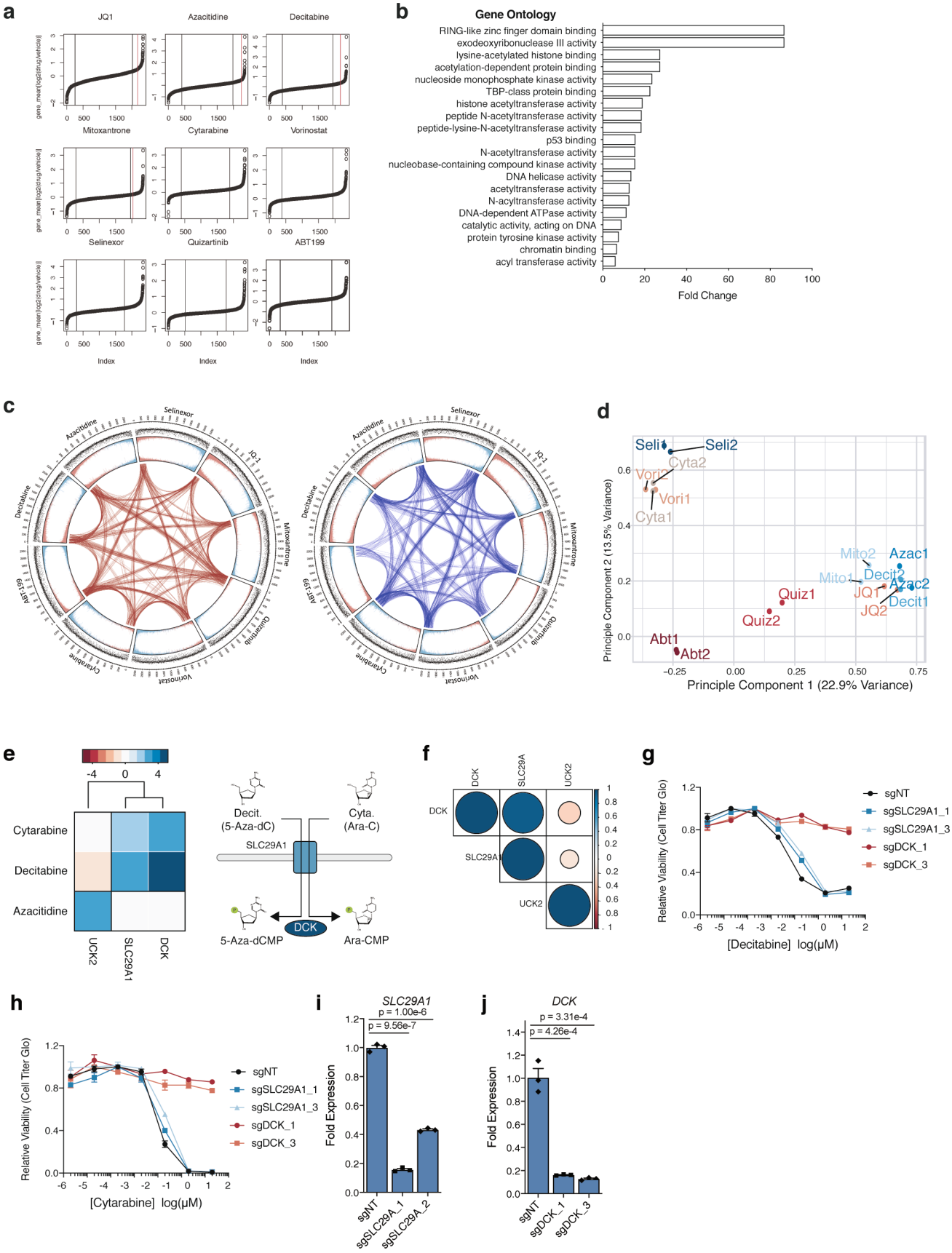

Extended Data Fig. 2 | See next page for caption.

Extended Data Fig. 2 | Additional analysis of drug-treated screens using API. a, Graphical depiction of scoring regions of nine drug modifier screens. Red lines indicate cutoff controlled at p-value 0.05. **b**, Gene ontology analysis of drug-induced AP genes ranked by fold-change. **c**, Circos plot displaying data from drug-modifier CRISPR screens as in Fig. 2a. **d**, PCA analysis of nine drug modifier screens conducted in n = 2 biologically independent experiments. Colors denote different drugs. **e**, Heatmap representing effect of sgRNAs targeting *DCK*, *UCK2*, *SLC29A1* on cytarabine, decitabine, and azacitidine; schematic depicts effect of DCK and SLC29A1 on deoxycytidines. **f**, Correlogram depicting Pearson correlation coefficients of *DCK*, *SLC29A1*, and *UCK2* depletion across nine drug modifier screens. **g**,**h**, Decitabine (**g**) and cytarabine (**h**) 8-point drug dilution series following CRISPR/Cas9 knockout of *SLC29A1* or *DCK* versus non-targeting control in OCI-AML2 cells. **i**,**j**, Fold-change of *SLC29A1* (**i**) and *DCK* (**j**) transcripts following CRISPR/Cas9 knockout of *SLC29A1* versus non-targeting control. P-values computed by two-sided two-sample t-Test for equal means. **g–j**, Data are mean ± SEM for n = 3 biologically independent experiments.

a

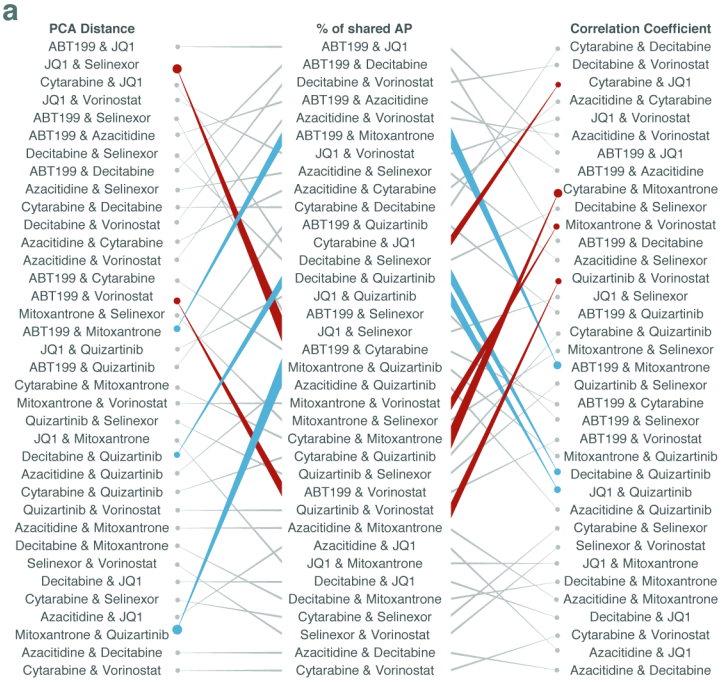

b

Pair	% AP	Corr. Coeff.	Distance
ABT199 and JQ1	75.610	-0.198	30.685
ABT199 and Decitabine	69.231	-0.142	24.299
Decitabine and Vorinostat	62.500	-0.261	21.786
ABT199 and Azacitidine	60.000	-0.193	25.233
Azacitidine and Vorinostat	59.184	-0.231	21.367
ABT199 and Mitoxantrone	57.143	-0.038	18.217
JQ1 and Vorinostat	55.556	-0.238	26.077
Azacitidine and Selinexor	52.941	-0.138	23.697
Azacitidine and Cytarabine	52.830	-0.249	21.536
Cytarabine and Decitabine	52.632	-0.262	22.013
ABT199 and Quizartinib	52.459	-0.081	16.376
Cytarabine and JQ1	50.000	-0.254	26.144
Decitabine and Selinexor	46.429	-0.160	24.519
Decitabine and Quizartinib	45.313	0.217	12.141
JQ1 and Quizartinib	43.860	0.230	17.462
ABT199 and Selinexor	41.429	0.066	26.038
JQ1 and Selinexor	41.304	-0.105	27.506
ABT199 and Cytarabine	41.096	0.059	20.311
Mitoxantrone and Quizartinib	40.984	0.159	5.123
Azacitidine and Quizartinib	38.983	0.258	12.128
Mitoxantrone and Vorinostat	38.182	-0.149	15.291
Mitoxantrone and Selinexor	37.931	-0.075	19.184
Cytarabine and Mitoxantrone	37.500	-0.172	15.655
Cytarabine and Quizartinib	34.940	-0.077	10.698
Quizartinib and Selinexor	30.769	-0.020	14.803
ABT199 and Vorinostat	30.667	0.105	19.505
Quizartinib and Vorinostat	28.235	-0.124	10.271
Azacitidine and Mitoxantrone	25.532	0.508	7.570
JQ1 and Mitoxantrone	25.000	0.450	13.117
Azacitidine and JQ1	25.000	0.564	5.563
Decitabine and JQ1	23.529	0.525	6.399
Decitabine and Mitoxantrone	14.583	0.506	7.248
Cytarabine and Selinexor	10.000	0.370	5.727
Selinexor and Vorinostat	9.756	0.395	6.534
Azacitidine and Decitabine	7.143	0.681	1.650
Cytarabine and Vorinostat	4.396	0.544	0.807

Extended Data Fig. 3 | Comparisons between API, PCA, and correlation. a, List of 36 drug pairs ranked by greatest PCA distance (left), greatest % of shared AP interactions (middle), and smallest Pearson correlation coefficient (right). Lines match drug pairs in each list. Drug pairs >10 positions lower in percent of shared AP interactions rank joined by red lines; drug pairs >10 positions higher in percent of shared AP interactions rank joined by blue lines. **b**, Percent of shared AP interactions, Pearson correlation coefficient and PCA distance for 36 drug pairs. **a**,**b**, Data from drug-modifier screens conducted in n = 2 biologically independent experiments.

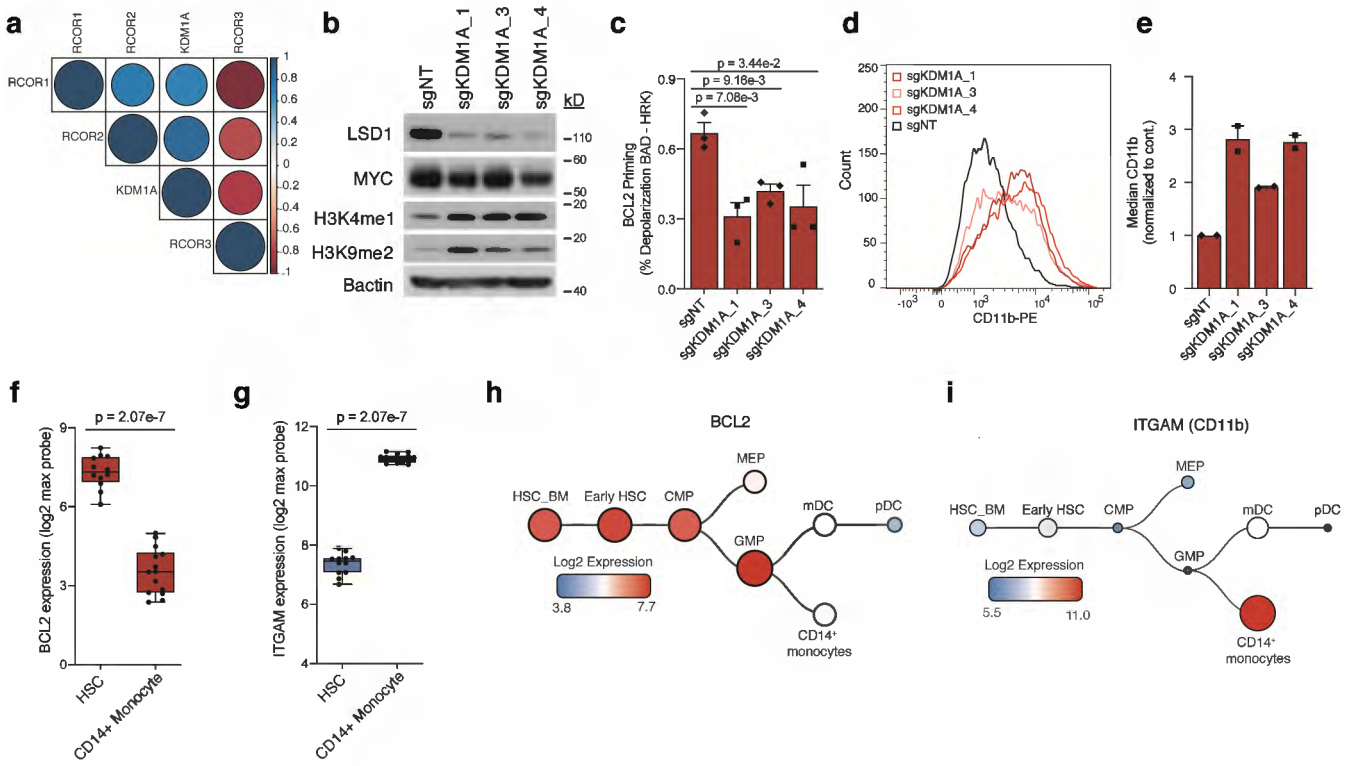

Extended Data Fig. 4 | *KDM1A* functions as a drug-induced AP gene by regulating differentiation. a, Correlogram depicting Pearson correlation coefficients of *KDM1A* and *RCOR1/2/3* depletion across nine drug modifier screens. Data from drug-modifier screens conducted in n = 2 biologically independent experiments. **b**, Immunoblot analysis of LSD1, MYC, H3K4me1 and H3K9me2 following CRISPR/Cas9 knockout of *KDM1A* in OCI-AML2 cells. Representative immunoblot of n = 3 independent experiments. Uncropped blots in Source Data. **c**, BH3 profiling of OCI-AML2 cells following CRISPR/Cas9 knockout of *KDM1A* versus non-targeting control. BCL2 priming defined as percent depolarization from HRK peptide (10μM) subtracted from percent depolarization from BAD (10μM) peptide. **d**,**e**, Flow-cytometry analysis of CD11b expression distribution (**d**) and median signal (**e**) in OCI-AML2 cells following CRISPR/Cas9 knockout of *KDM1A* versus non-targeting control. Median signal normalized to non-targeting control sgRNA. Data are mean ± SEM for n = 2 biologically independent experiments. **f–i**, BCL2 (**f**, **h**) and CD11b (encoded by *ITGAM*) (**g**, **i**) expression in hematopoietic stem cells (HSC; n = 11), common myeloid progenitors (CMP, n = 3), megakaryocyte-erythroid progenitor cell (MEP, n = 3), granulocyte monocyte progenitors (GMP, n = 3), CD11c+ myeloid dendritic cells (mDC, n = 5), CD123+ plasmacytoid dendritic cells (pDC, n = 5), and CD14+ monocytes (n = 13) from BloodSpot using HemaExplorer dataset. Sample size refers to biologically independent samples. Data are log2 expression of highest intensity microarray probe. Boxplot elements defined in Methods. **c**,**f**,**g**; P-values computed by two-sided two-sample t-Test for equal means. **c**,**e**,**f**,**g**; Data are mean ± SEM for n = 3 biologically independent experiments.

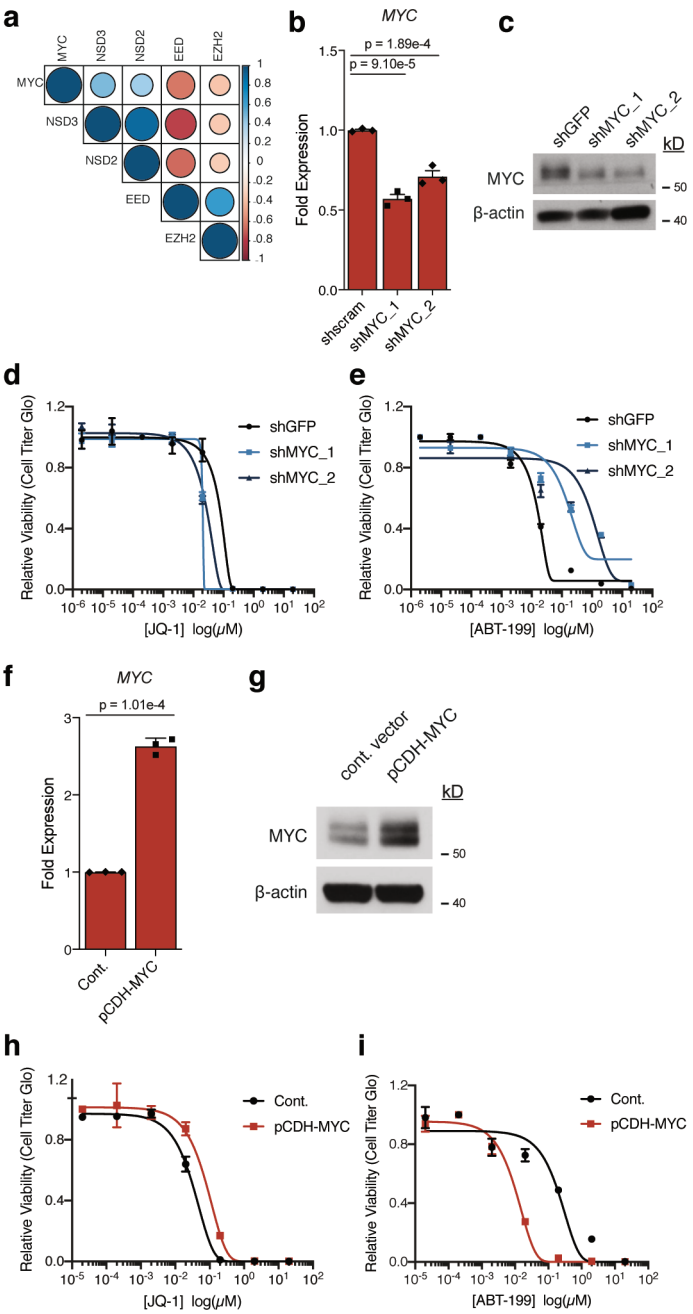

Extended Data Fig. 5 | *MYC* is a drug-induced AP gene. a, Correlogram depicting Pearson correlation coefficients of *MYC*, *NSD3*, *NSD2*, *EED* and *EZH2* depletion values across nine drug modifier screens. Data from drug-modifier screens conducted in n = 2 biologically independent experiments. **b**,**c**, Confirmation of *MYC* shRNA knockdown in OCI-AML2 by transcript (**b**) and protein (**c**). Representative immunoblot of n = 3 independent experiments. **d**,**e**, JQ-1 (**d**) and ABT-199 (**e**) 8-point drug dilution series following shRNA knockdown of MYC in OCI-AML2 cells. **f**,**g**, Confirmation of MYC overexpression in OCI-AML2 by transcript (**f**) and protein (**g**). Representative immunoblot of n = 3 independent experiments. **h**,**i**, JQ-1 (**h**) and ABT-199 (**i**) 8-point drug dilution series following overexpression of MYC in OCI-AML2 cells. **b**,**f**; P-values computed by two-sided two-sample t-Test for equal means. **b**,**d–f**,**h**,**i**, Data are mean ± SEM for n = 3 biologically independent experiments. Uncropped blots in Source Data.

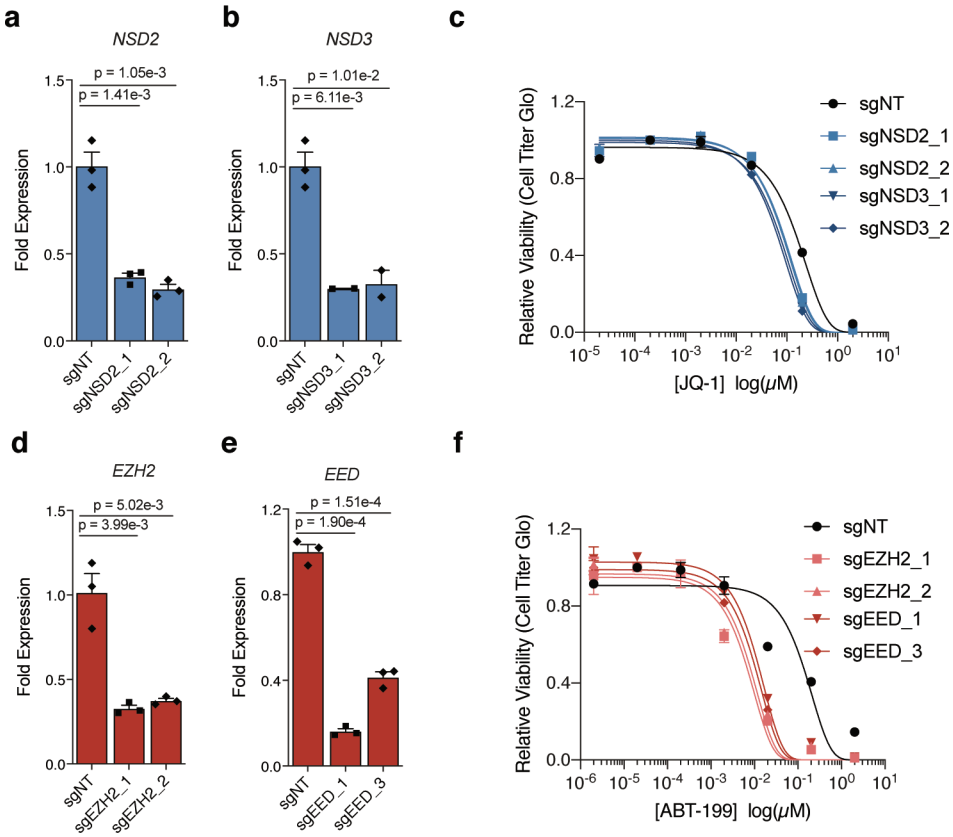

Extended Data Fig. 6 | EZH2/EED/NSD2/NSD3 modulate JQ-1 and ABT-199 sensitivity through MYC. a,**b**; **d**,**e**, Relative expression of *NSD2* (**a**), *NSD3* (**b**), *EZH2* (**d**), and *EED* (**e**) transcripts in cells with CRISPR/Cas9 knockout. P-values computed by two-sided two-sample t-Test for equal means. Data are presented as mean ± SEM for n = 3 biologically independent experiments. **c**,**f**, 8-point dose-response curves of JQ-1 (**c**) and ABT-199 (**f**) following CRISPR/Cas9 knockout of *NSD2/3* (**c**) and *EZH2* or *EED* (**f**). Data are presented as mean ± SEM for n = 3 biologically independent experiments.

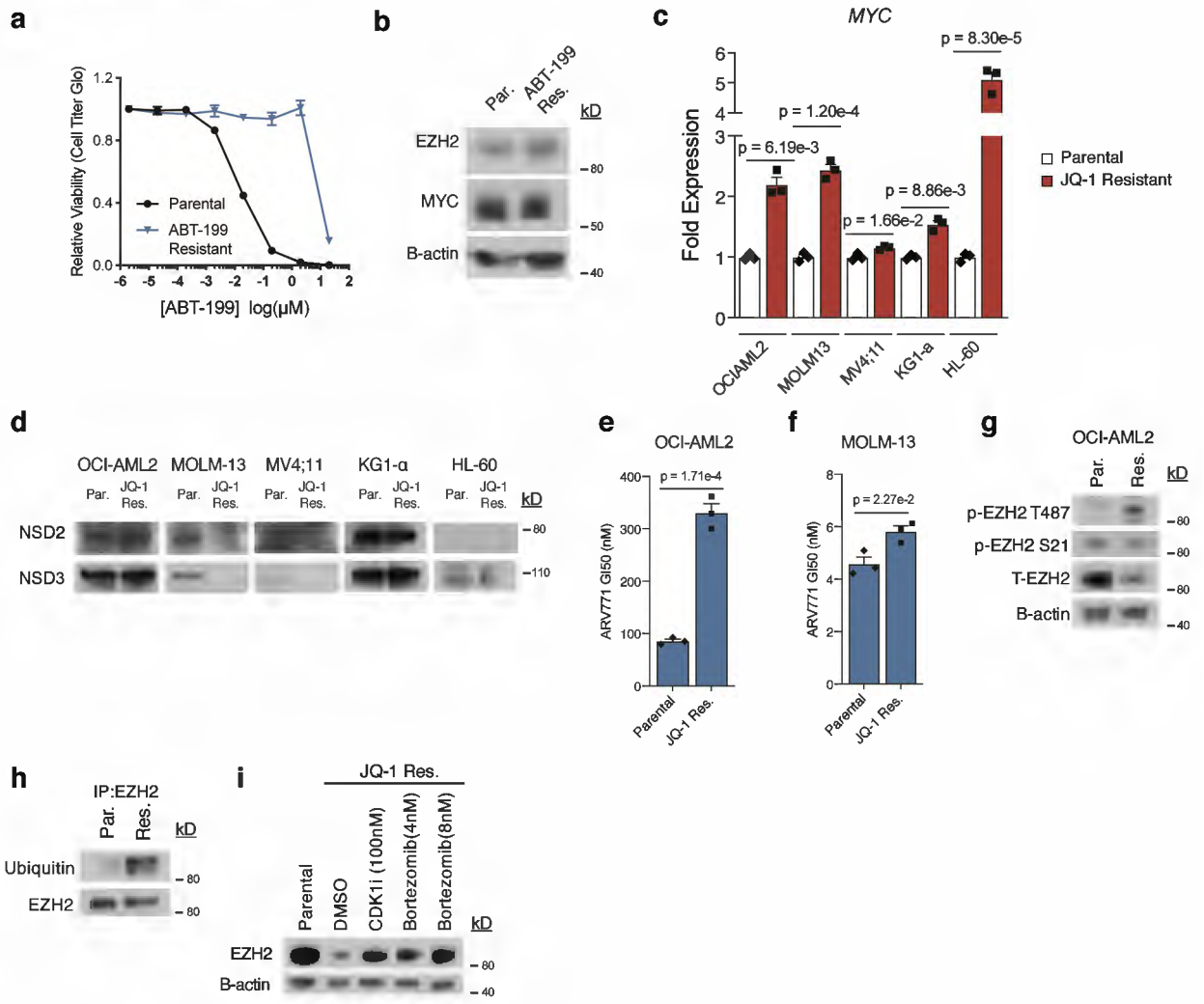

Extended Data Fig. 7 | Additional characterization of ABT-199 and JQ-1-resistant AML cells. a, 8-point dose-response curves of ABT-199 in parental and ABT-199-resistant OCI-AML2 cells. **b**, Immunoblot analysis of EZH2 and MYC in parental and ABT-199-resistant OCI-AML2 cells. **c**, Fold-change of *MYC* transcripts across matched parental and JQ-1-resistant AML cell lines. **d**, Immunoblot analysis of NSD2 and NSD3 across matched parental and JQ-1 resistant AML cell lines. **e**,**f**, ARV771 GI_{50} values of parental and JQ-1-resistant OCI-AML2 (**e**) and MOLM-13 (**f**). **g**, Immunoblot analysis of phosphorylated EZH2 at T487 and S21 in parental and JQ-1 resistant OCI-AML2 cells. **h**, Immunoblot analysis of ubiquitin and EZH2 following immunoprecipitation of EZH2 in OCI-AML2 cells. **i**, Immunoblot analysis of EZH2 following treatment of JQ-1 resistant OCI-AML2 cells with CDK1 inhibitor (CDK1i) or proteasome inhibitor (Bortezomib) for 24 hours. **a**,**c**,**e**,**f**; Data are mean ± SEM for n = 3 biologically independent experiments. **c**,**e**,**f**; P-values computed by two-sided two-sample t-Test for equal means. **b**,**d**,**g–i**; Representative immunoblots of n = 3 independent experiments. Uncropped blots in Source Data.

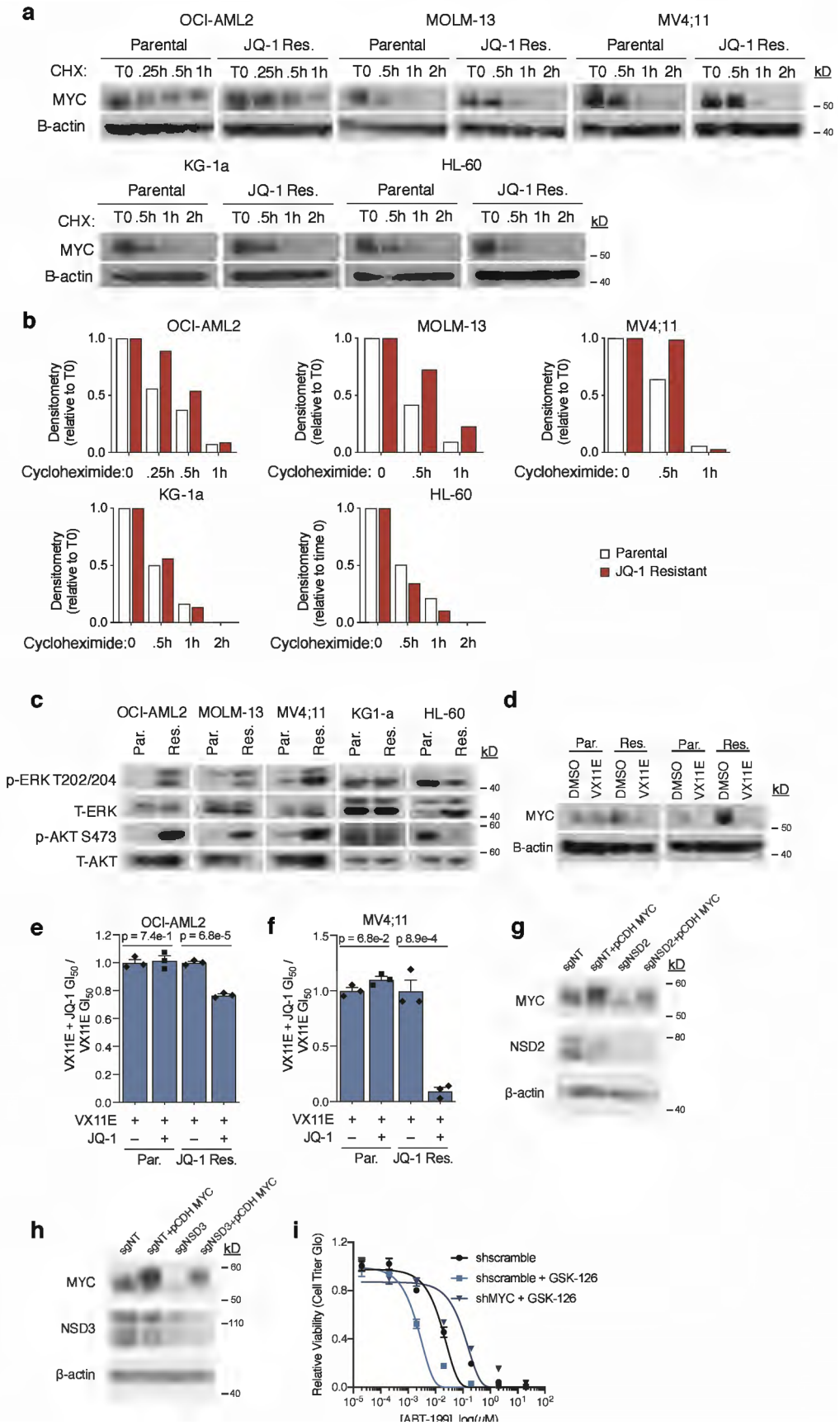

Extended Data Fig. 8 | See next page for caption.

Extended Data Fig. 8 | MYC upregulation in JQ-1-resistant cells can be driven by AKT/ERK. a,**b**, Immunoblot analysis of MYC (**a**) in matched parental and JQ-1 resistant AML cells following treatment with 20μg/mL cycloheximide (CHX) for indicated times. Quantification by densitometry (**b**) normalized to time zero signal. **c**, Immunoblot analysis of phosphorylated ERK at T202/204 and phosphorylated AKT at S437 in parental and JQ-1 resistant AML cells relative to total proteins. **d**, Immunoblot analysis of MYC in parental and JQ-1 resistant OCI-AML2 and MV4;11 cells treated with VX11E for 24 hours. OCI-AML2 cells treated with 500nM VX11E and MV4;11 cells treated with 2μM VX11E. **e**,**f**, GI_{50} value of VX11E in combination with 100nM JQ-1 normalized to VX11E alone in parental and JQ-1 resistant OCI-AML2 (**e**) and MV4;11 (**f**) cells. **g**,**h**, Immunoblot analysis of MYC, NSD2 (**g**) and NSD3 (**h**) in OCI-AML2 cells following overexpression of pCDH-MYC in combination with sgRNAs targeting NSD2 (**g**) and NSD3 (**h**). **i**, ABT-199 8-point drug dilution series following shRNA knockdown of MYC in combination with GSK-126. **e**,**f**,**i**; Data are mean ± SEM for n = 3 biologically independent experiments. **e**,**f**; P-values computed by two-sided two-sample t-Test for equal means. **a**,**c**,**d**,**g**,**h**; Representative immunoblots of n = 3 independent experiments. Uncropped blots in Source Data.

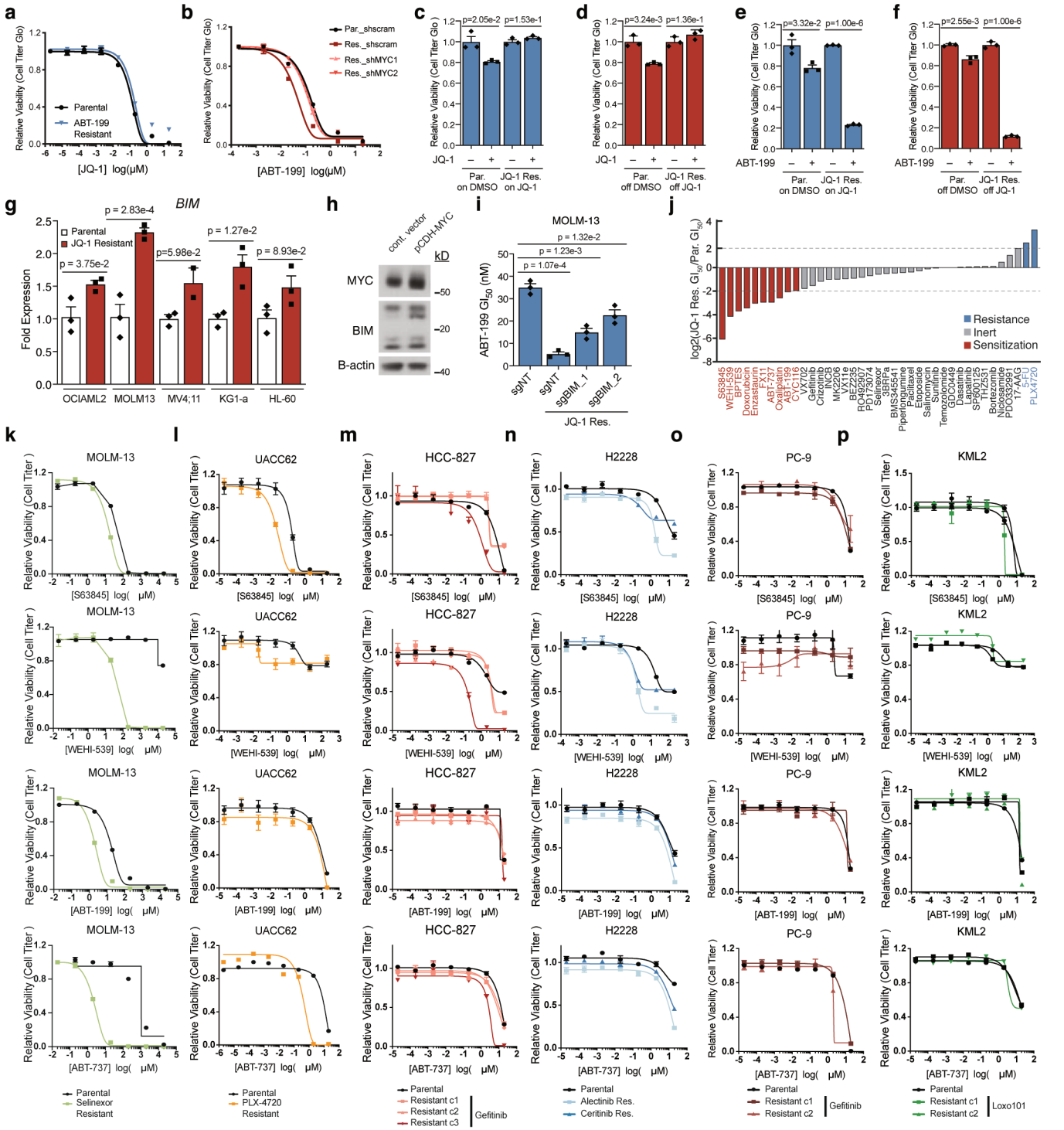

Extended Data Fig. 9 | See next page for caption.

Extended Data Fig. 9 | JQ-1-resistant AML cells harbor widespread BIM-related collateral sensitivities. a, 8-point dose-response curves of JQ-1 in parental and ABT-199-resistant OCI-AML2 cells. **b**, 8-point dose-response curves of ABT-199 in JQ-1-resistant OCI-AML2 cells following shRNA knockdown of MYC. **c**,**d**, Effect of 72-hour, 200nM JQ-1 treatment on cell viability of parental and JQ-1 resistant OCI-AML2 cultured continuously in JQ-1 (**c**) or taken off JQ-1 for 10 days (**d**), normalized to effect of vehicle treatment. **e**,**f**, Effect of 72-hour, 2nM ABT-199 treatment on cell viability of parental and JQ-1-resistant OCI-AML2 cells cultured continuously in JQ-1 (**e**) or taken off JQ-1 for 10 days (**f**), normalized to effect of vehicle treatment. **g**, Fold-change of BIM transcripts across matched parental and JQ-1 resistant AML cell lines. **h**, Immunoblot of MYC and BIM following overexpression of pCDH-MYC in OCI-AML2; representative of n = 1 independent experiments. Uncropped blots in Source Data. **i**, ABT-199 GI_{50} in parental and JQ-1 resistant MOLM-13 cells following CRISPR/Cas9 knockout of BIM or non-targeting control. **j**, Specification of 40 compound drug screen in JQ-1 resistant OCI-AML2 cells relative to parental. **k–p**, 8-point dose-response curves in parental and drug resistant cell line derivatives. **q**, Gating strategy for flow cytometric analysis of murine bone marrow aspirate. **c–g**; **i**, P-values computed by two-sided two-sample t-Test for equal means. **a–g**; **i–p**, Data are mean ± SEM for n = 3 biologically independent experiments.

nature research

Corresponding author(s): Dr. Kris C. Wood

Last updated by author(s): Jan 27, 2020

Reporting Summary

Nature Research wishes to improve the reproducibility of the work that we publish. This form provides structure for consistency and transparency in reporting. For further information on Nature Research policies, see Authors & Referees and the Editorial Policy Checklist.

Statistics

For all statistical analyses, confirm that the following items are present in the figure legend, table legend, main text, or Methods section.

n/a	Confirmed	
☐	☒	The exact sample size (*n*) for each experimental group/condition, given as a discrete number and unit of measurement
☐	☒	A statement on whether measurements were taken from distinct samples or whether the same sample was measured repeatedly
☐	☒	The statistical test(s) used AND whether they are one- or two-sided *Only common tests should be described solely by name; describe more complex techniques in the Methods section.*
☐	☒	A description of all covariates tested
☐	☒	A description of any assumptions or corrections, such as tests of normality and adjustment for multiple comparisons
☐	☒	A full description of the statistical parameters including central tendency (e.g. means) or other basic estimates (e.g. regression coefficient) AND variation (e.g. standard deviation) or associated estimates of uncertainty (e.g. confidence intervals)
☐	☒	For null hypothesis testing, the test statistic (e.g. *F*, *t*, *r*) with confidence intervals, effect sizes, degrees of freedom and *P* value noted *Give P values as exact values whenever suitable.*
☒	☐	For Bayesian analysis, information on the choice of priors and Markov chain Monte Carlo settings
☒	☐	For hierarchical and complex designs, identification of the appropriate level for tests and full reporting of outcomes
☒	☐	Estimates of effect sizes (e.g. Cohen's *d*, Pearson's *r*), indicating how they were calculated

Our web collection on statistics for biologists contains articles on many of the points above.

Software and code

Policy information about availability of computer code

Data collection	Real-time qPCR: CFX384 Touch Real-Time PCR Detection System Cell Counting: Z2 Coulter Particle Count and Size Analyzer Plate Reader for luminescence assays: TECAN infinite M1000Pro Blot image scanning: Epson Perfection V600 Photo DNA/RNA concentration measurement: Thermo Fisher NanoDrop Lite FACS Analysis: Becton Dickinson FACSCanto II
Data analysis	GraphPad Prism 8.0.2 GraphPad Prism 7.0 Microsoft Excel 2016 Microsoft Word 2016 RStudio Version 1.1.463 R version 3.5.1 Adobe Illustrator CC 2017 FlowJo 10.6.0 EPSON Scan 3.9.4 Circos (http://circos.ca/) GeneOnology (http://geneontology.org) BloodSpot HemaExplorer (http://servers.binf.ku.dk/bloodspot/)

For manuscripts utilizing custom algorithms or software that are central to the research but not yet described in published literature, software must be made available to editors/reviewers. We strongly encourage code deposition in a community repository (e.g. GitHub). See the Nature Research guidelines for submitting code & software for further information.

Data

Policy information about availability of data

All manuscripts must include a data availability statement. This statement should provide the following information, where applicable:

- Accession codes, unique identifiers, or web links for publicly available datasets
- A list of figures that have associated raw data
- A description of any restrictions on data availability

The data supporting the findings of this study are found within the paper and supplementary files. Depletion values for CRISPR/Cas9 drug-modifier screens depicted in figures 2, S2 and S3 are provided in supplementary table 2. Custom script for analyzing CRISPR/Cas9 screens and calculating API is available upon request.

Field-specific reporting

Please select the one below that is the best fit for your research. If you are not sure, read the appropriate sections before making your selection.

☒ Life sciences ☐ Behavioural & social sciences ☐ Ecological, evolutionary & environmental sciences

For a reference copy of the document with all sections, see nature.com/documents/nr-reporting-summary-flat.pdf

Life sciences study design

All studies must disclose on these points even when the disclosure is negative.

Sample size	Sample size calculations were not performed. All in vitro experiments were conducted as three biologically independent experiments. n = 3 was selected in order to balance sufficiency for calculating relevant test statistics with the cost and feasibility of performing multiplexed experiments. For mouse study, sample size was chosen based on historical demonstration that the in vivo models were highly penetrant and consistent.
Data exclusions	No data were excluded from analysis.
Replication	CRISPR screens were performed in replicate. Experimental findings were reproduced by multiple individuals and/or multiple biologically independent experiments with similar results.
Randomization	Mice were randomized twelve days after injection.
Blinding	To establish humane endpoint for mouse study, blinded observers visually inspected mice for obvious signs of distress, such as loss of appetite, hunched posture.

Reporting for specific materials, systems and methods

We require information from authors about some types of materials, experimental systems and methods used in many studies. Here, indicate whether each material, system or method listed is relevant to your study. If you are not sure if a list item applies to your research, read the appropriate section before selecting a response.

Materials & experimental systems

n/a	Involved in the study
☐	☒ Antibodies
☐	☒ Eukaryotic cell lines
☒	☐ Palaeontology
☐	☒ Animals and other organisms
☐	☒ Human research participants
☒	☐ Clinical data

Methods

n/a	Involved in the study
☒	☐ ChIP-seq
☐	☒ Flow cytometry
☒	☐ MRI-based neuroimaging

Antibodies

Antibodies used	B-actin [13E5] (CST #4970, Lot 15, 1:3000), Myc [Y69] (Abcam ab32072, GR323270322, 1:1000), Ezh2 [D2C9] (CST #5246, Lot 9, 1:1000), Acetyl-Histone H3 (Lys27) [D5E4] (CST #8173, Lot 8, 1:1000), Bim [C34C5] (CST #2933, Lot 8, 1:500), Puma [D30C10] (CST #12450, Lot 3 1:500), Noxa [D8L7U] (CST #14766, Lot 1, 1:500), Bcl-2 [D55G8] (CST #4223, Lot 2, 1:1000), Mcl-1 [D35A5] (CST #5453, Lot 4, 1:1000), Bcl-xL [54H6] (CST #2764, Lot 6, 1:1000), Nsd2 [29D1] (Abcam ab75359 1:500), Nsd3 [Polyclonal] (Abcam ab4514, GR3199834-1, 1:500), LSD1 [Polyclonal] (CST #2139, Lot 5, 1:1000), H3K4me1 [Polyclonal] (Abcam ab8895 1:2000), H3K9me2 [D85B4] (CST #4658, Lot 5, 1:1000), phospho-AKT (Ser473) [D9E] (CST #4060, Lot 7, 1:1000), AKT [C67E7] (CST #4691, Lot 20, 1:1000), Phospho-p44/42 MAPK (Erk1/2) (Thr202/Tyr204) [D13.14.4E] (CST #4370S, Lot 3, 1:1000), p44/42 MAPK (Erk1/2) [137F5] (CST #4695, Lot 2, 1:1000), CD11b-PE antibody [M1/70] (BioLegend #101207, Lot B277814, 1:500), APC anti-

	human CD45 [2D1] (BioLegend #368512, Lot 2034153, 3:100), PE-Cy7 anti-human CD13 [WM-15] (eBioscience #25-0138-42, Lot 2065232, 3:100), PE-Cy7 anti-human CD33 [WM-53] (eBioscience, 25-0338-42, Lot 1918586, 3:100)
Validation	All antibodies have been validated by supplier to detect the human protein of interest by western immunoblotting.

Eukaryotic cell lines

Policy information about cell lines

Cell line source(s)	HCC827, PC-9, KM-12, MOLM-13, OCI-AML2, MV4;11, KG-1a, HL-60 and UACC-62 cells were purchased from American Type Culture Collection (ATCC) or Duke University Cell Culture Facility (CCF).
Authentication	All cell lines were authenticated prior to use using STR profiling.
Mycoplasma contamination	All cell lines were confirmed as mycoplasma-free upon receipt.
Commonly misidentified lines (See ICLAC register)	No cell lines were misclassified. No commonly misclassified cell lines were used, according to the ICLAC register of commonly misidentified cell lines.

Animals and other organisms

Policy information about studies involving animals; ARRIVE guidelines recommended for reporting animal research

Laboratory animals	Mus Musculus, NOD.Cg-Prkdcscid Il2rgtm1Sug Tg(SV40/HTLV-IL3,CSF2)10-7Jic/JicTac, male, 6-8 week old.
Wild animals	No wild animals were used in this study.
Field-collected samples	No samples collected from the field were used in this study.
Ethics oversight	The French National Ethics Committee on Animal Care reviewed and approved all mouse experiments described in this study. Authorization number: APAFIS#8909-2017021413452743 v1

Note that full information on the approval of the study protocol must also be provided in the manuscript.

Human research participants

Policy information about studies involving human research participants

Population characteristics	Patient-derived xenograft (PDX) model of AML derived from a 57-year-old women with therapy-related AML. Patient was found to have t(9;11)(p22;q23) MLL-AF9 positive blasts with M5a pathology.
Recruitment	Primary patient AML blasts were collected from bone marrow aspirates or peripheral blood samples after obtaining patient informed consent under Saint-Louis Hospital Internal Review Board-approved protocols (IRB00003888). Dry pellets and frozen viable cells were stored in a Saint-Louis Hospital's biobank, coordinated by Pr. Anne Janin, which has accreditation from the French National Cancer Institute (INCA).
Ethics oversight	Saint-Louis Hospital Internal Review Board (IRB00003888)

Note that full information on the approval of the study protocol must also be provided in the manuscript.

Flow Cytometry

Plots

Confirm that:

☒ The axis labels state the marker and fluorochrome used (e.g. CD4-FITC).

☒ The axis scales are clearly visible. Include numbers along axes only for bottom left plot of group (a 'group' is an analysis of identical markers).

☒ All plots are contour plots with outliers or pseudocolor plots.

☒ A numerical value for number of cells or percentage (with statistics) is provided.

Methodology

Sample preparation	Bone marrow cells were washed in PBS prior to staining with either an APC-coupled anti-human-CD45 or a cocktail of PE-Cy7-coupled anti-human CD13/CD33 antibodies resuspended in 0.5% BSA, 2mM EDTA PBS.
Instrument	Data collection was performed on Becton Dickinson FACScanto II instrument.
Software	Becton Dickinson DIVA software.

Cell population abundance	The fraction of human cells in mouse bone marrow may vary depending on the treatment applied to the mice. The goal of our experiments was to assess by flow cytometry the remaining proportion of human cell population in response to treatment.
Gating strategy	Live cells were gated on an FSC / SSC scatter plot. Singlets were gated on an FSC-H / FSC-A scatter plot. Proportion of CD45- or CD13/33-positive human cells was then assessed on the singlet population.

☒ Tick this box to confirm that a figure exemplifying the gating strategy is provided in the Supplementary Information.